*remote sensing*

MDPI

*Article*

# A New Orbiting Deployable System for Small Satellite Observations for Ecology and Earth Observation

**Elena Martellato [1,*], Alice Maria Piccirillo [1], Giampaolo Ferraioli [1], Alessandra Rotundi [1,2], Vincenzo Della Corte [2], Pasquale Palumbo [1,2], Emanuele Alcaras [1], Luca Appolloni [1], Giuseppe Aulicino [1], Ivano Bertini [1], Vincenzo Capozzi [1], Elena Catucci [1], Zelia Dionnet [3], Pasquale Di Palma [1], Flavio Esposito [1], Emanuele Ferrentino [1], Anna Innac [1], Laura Inno [1], Silvia Pennino [1], Simona Saviano [1,4], Giuseppina Tirimberio [1,5], Stefania Campopiano [1], Elena Chianese [1], Pier Paolo Franzese [1], Giannetta Fusco [1], Salvatore Gaglione [1], Agostino Iadicicco [1], Ferdinando Nunziata [1], Claudio Parente [1], Vincenzo Piscopo [1], Angelo Riccio [1], Giovanni Fulvio Russo [1] and Enrico Zambianchi [1]**

[1] Department of Sciences and Technologies, University of Napoli "Parthenope", Centro Direzionale Isola C4, 80143 Napoli, Italy; alicemaria.piccirillo001@studenti.uniparthenope.it (A.M.P.); giampaolo.ferraioli@uniparthenope.it (G.F.); rotundi@uniparthenope.it (A.R.); pasquale.palumbo@uniparthenope.it (P.P.); emanuele.alcaras@studenti.uniparthenope.it (E.A.); luca.appolloni@collaboratore.uniparthenope.it (L.A.); giuseppe.aulicino@uniparthenope.it (G.A.); ivano.bertini@uniparthenope.it (I.B.); vincenzo.capozzi@collaboratore.uniparthenope.it (V.C.); elena.catucci@uniparthenope.it (E.C.); pasquale.dipalma@collaboratore.uniparthenope.it (P.D.P.); flavio.esposito@collaboratore.uniparthenope.it (F.E.); emanuele.ferrentino@uniparthenope.it (E.F.); anna.innac@collaboratore.uniparthenope.it (A.I.); laura.inno@uniparthenope.it (L.I.); silvia.pennino@uniparthenope.it (S.P.); simona.saviano@collaboratore.uniparthenope.it (S.S.); giuseppina.tirimberio@unicampania.it (G.T.); stefania.campopiano@uniparthenope.it (S.C.); elena.chianese@uniparthenope.it (E.C.); pierpaolo.franzese@uniparthenope.it (P.P.F.); giannetta.fusco@uniparthenope.it (G.F.); salvatore.gaglione@uniparthenope.it (S.G.); agostino.iadicicco@uniparthenope.it (A.I.); ferdinando.nunziata@uniparthenope.it (F.N.); claudio.parente@uniparthenope.it (C.P.); vincenzo.piscopo@uniparthenope.it (V.P.); angelo.riccio@uniparthenope.it (A.R.); giovanni.russo@uniparthenope.it (G.F.R.); enrico.zambianchi@uniparthenope.it (E.Z.)

[2] Institute for Space Astrophysics and Planetology, National Institute for Astrophysics, Via Fosso del Cavaliere 100, 00133 Roma, Italy; vincenzo.dellacorte@inaf.it

[3] Institut d'Astrophysique Spatiale, Université Paris-Saclay, Centre National de la Recherche Scientifique, Bat 120-121, 91405 Orsay, France; zelia.dionnet@universite-paris-saclay.fr

[4] Department of Research Infrastructures for Marine Biological Resources, Stazione Zoologica Anton Dohrn, Villa Comunale, 80121 Naples, Italy

[5] Department of Mathematics and Physics, University of Campania, Viale Lincoln, 5, 81100 Caserta, Italy

* Correspondence: elena.martellato@collaboratore.uniparthenope.it

**Abstract:** In this paper, we present several study cases focused on marine, oceanographic, and atmospheric environments, which would greatly benefit from the use of a deployable system for small satellite observations. As opposed to the large standard ones, small satellites have become an effective and affordable alternative access to space, owing to their lower costs, innovative design and technology, and higher revisiting times, when launched in a constellation configuration. One of the biggest challenges is created by the small satellite instrumentation working in the visible (VIS), infrared (IR), and microwave (MW) spectral ranges, for which the resolution of the acquired data depends on the physical dimension of the telescope and the antenna collecting the signal. In this respect, a deployable payload, fitting the limited size and mass imposed by the small satellite architecture, once unfolded in space, can reach performances similar to those of larger satellites. In this study, we show how ecology and Earth Observations can benefit from data acquired by small satellites, and how they can be further improved thanks to deployable payloads. We focus on DORA—Deployable Optics for Remote sensing Applications—in the VIS to TIR spectral range, and on a planned application in the MW spectral range, and we carry out a radiometric analysis to verify its performances for Earth Observation studies.

check for updates

**Citation:** Martellato, E.; Piccirillo, A.M.; Ferraioli, G.; Rotundi, A.; Della Corte, V.; Palumbo, P.; Alcaras, E.; Appolloni, L.; Aulicino, G.; Bertini, I.; et al. A New Orbiting Deployable System for Small Satellite Observations for Ecology and Earth Observation. *Remote Sens.* **2022**, *14*, 2066. https://doi.org/10.3390/rs14092066

Academic Editor: Michael Obland

Received: 28 January 2022
Accepted: 20 April 2022
Published: 26 April 2022

**Publisher's Note:** MDPI stays neutral with regard to jurisdictional claims in published maps and institutional affiliations.

**Keywords:** Earth Observation; remote sensing; deployable payload; optical instruments; radars; ocean; atmosphere; ecology

## 1. Introduction

Remote sensing, from visible (VIS), through thermal infrared (TIR), up to microwaves (MW), represents a key tool to study and monitor our planet, especially when field measurements are hard to produce because of environmental coverage (e.g., oceans) and/or technical and operational issues (e.g., inaccessibility, or seasonal or annual variations). Remote sensing multispectral data are critical to monitor the results of human activities, e.g., polluting gases or industry-made products, and natural hazards, e.g., hurricanes, floods, fires, earthquakes, volcanic eruptions, sandstorms, soil erosions, and landslides [1–14], whereas the availability of more frequent views over the same area allows for a better management of natural hazards and disaster e.g., [15]. These datasets allow for the development of strategies for the safeguarding of natural habitats, plants, and animal species (e.g., [16–20]).

Although a great return is guaranteed, remote sensing performed by standard satellites is very expensive [21], and is thus affordable only to countries and large consortia able to ensure expensive, long-term operations. The high costs are due to large volumes and masses (>1 $m^3$, >500 kg) of the standard satellites, which imply the need for powerful launchers. In the late 1980s, the technological advancement of small satellites [22], classified in different classes depending on their masses (cf. Table 1), allowed for space programs to also become accessible to countries, communities, and private institutes with limited funding (e.g., [23]). Furthermore, small satellites represent ideal platforms to test and validate new, cutting-edge technologies. The limited on-board resources indeed require innovative propulsion methods (including electric propulsion and compressed gas or liquids, e.g., butane and carbon dioxide), attitude control, communication, and computation systems. Micro-satellites use innovative compact communication systems (e.g., optical transceivers, antenna arrays, and satellite-to-satellite data relay), in the VHF (very high frequency), UHF (ultra high frequency), and L-, S-, C-, and X-bands. In particular, a remote sensing payload operating in VIS, TIR, and MW onboard small satellites represents a great challenge to balance miniaturization and performance, because the achieved resolution depends on the size of the signal collector. A novel solution is offered by the deployable approach, which allows to both minimize the instrument volume at the launch phase and achieve good performances at the orbital phase (once unfolded). For Earth Observations (EO), deployable optics can become an asset to gain those accurate, precise, and frequent measurements required to keep monitoring natural and human activities [24]. Alongside any technical arrangements, the increasingly widespread data fusion techniques rely on merging data from different sensors to ameliorate the quality of the final output, as regards spatial resolution, geometry, and topography (e.g., [25]).

**Table 1.** Small satellite classification according to their mass adapted from [21,26,27].

| Small Satellite Class | Mass [kg] |
|---|---|
| Mini | 100 to 500 |
| Micro | 10 to 100 |
| Nano | 1 to 10 |
| Pico | 0.1 to 1 |
| Femto | <0.1 |

In this paper, we reviewed several marine and atmospheric studies, as representative cases (i) to highlight the improvements in accuracy, resolution, and spatial/time coverage when using remote sensing payload onboard small satellites, and (ii) to validate the performances of a deployable telescope, currently under development, targeting ecological questions. In Section 2, we present a short introduction about both small satellites and

remote sensing payloads for EO, along with DORA, the new deployable system that is investigated in this study. In Section 3, environmental studies, focused on the potential ecological hazards to the habitat, are described: for each application and observation strategy, the most favorable characteristics of the satellite are defined. In Section 4, we introduce the data fusion techniques as a powerful tool to combine multisensory data to better analyze a given topic. In Section 5, we illustrate the radiometric analysis carried out to evaluate the performances of the deployable telescope. Finally, in Section 6, conclusions and future perspectives are outlined.

## 2. Small Satellites for VIS, TIR, and MW Remote Sensing

Satellites can be classified according to their weight: large (mass > 1000 kg), medium (mass from 500 kg to 1000 kg), and small (mass < 500 kg). Small satellites, born as a mere curious experiment and which currently have a key role for space exploration [22,26,27], can be further classified, as reported in Table 1.

### *2.1. Evolution of Small Satellites*

The historical evolution of small satellites has been extensively presented in a number of other works (e.g., [22,28–31]); here we aim to provide only the main phases in order to contextualize our work.

Small satellites were pioneered by a group of radio amateurs in California, who, in 1961, built and launched a 10 kg satellite, OSCAR-1 [32]. The first advance came in the subsequent years, with the addition of solar cells and rechargeable batteries, to allow small satellites to achieve useful lifetimes in orbit, and rudimentary attitude stabilization techniques (e.g., U.K. MoD Prospero, 66 kg, 1971). The transition to the "modern" small satellites occurred in 1981 with the launch of the 54 kg micro-satellite UoSAT-1 (University of Surrey Satellite), which included two in-orbit, reprogrammable microcomputers. UoSAT-1 was the first civilian satellite built to assess the feasibility of the design, construction, and launch of a scientific small satellite at a low cost. The U.S. Department of Defense started a LightSat initiative in the mid-1980s with the goal of reducing the costs and development time of satellites in the 50 to 1000 kg range [33]. During the 1980s, micro-satellites were considered of interest, but only for education and training.

At the beginning of the 1990s, a number of commercial proposals were advanced for constellations of small satellites operating in low Earth orbit (LEO), in order to provide worldwide communications, focusing on services not provided by the geostationary Earth orbit (GEO) satellites. During the 1990s, micro-satellites were used for technology demonstration and the verification of new digital services, before the widespread deployment of terrestrial infrastructure, rudimentary EO, radio science, military applications, and training programs for developing space nations. A series of micro-satellites, developed at the Surrey Space Centre [34], demonstrated steadily improved EO capabilities, e.g., KITSat [35], designed for experimental satellite engineering, PoSAT [36,37], 1 km ground sampling distance (GSD) for NIR, Thai-Phutt [22,38], and the first multispectral imaging micro-satellite to achieve 300 m GSD NIR, Red, Green, and Blue, FASat-Bravo, that carried instruments to monitor the distribution and concentrations of the ozone [39].

Between the end of the 1990s and the beginning of the 2000s, the complexity and potential of small satellite development was encouraged by a series of international collaborations between emerging nations aiming to an affordable access to space. Modern small satellites have, therefore, become suitable for EO, especially via constellations, due to advancing technology and the lowering of costs of production. This was the case, for instance, for the Disaster Monitoring Constellation First Generation (DMC-1G), an international partnership based on a Know-How Transfer and Training program for Third Countries, featuring expense and problem sharing, and remote sensing data exchange between all the partners. The DMC-1G constellation was made up by five micro-satellites (~100 kg each), which were launched within a time window from 2002 to 2005, into a

686 km sun-synchronous orbit (SSO), and resulted in being particularly effective during the large-scale Indian Ocean Tsunami (2004) and Hurricane Katrina (2005) disasters [40].

The combination of commercial appeal and low unit cost brought small satellites to the center of attention in 2010, and stimulated proposals for new applications and business models [22]. The advent of small satellite constellations coupled to the Internet, Cloud storage, advanced processing, and distribution methods has fostered the change from science to commodity. The evolution of small satellite EO companies, e.g., RapidEye, SkyBox, BlackBridge, and Planet (Labs), has demonstrated the rapid changes and their market volatility. Specifically, RapidEye was operative since 2008 until a couple of years ago. It represented a major milestone in the EO industry, for being the first fully commercial operational class EO system using a constellation of five micro-satellites (~150 kg), which provided exceptional performance for their class and a full end-to-end system. A dedicated Spacecraft Control Centre and an 80 Mb/s X-band data downlink ground station service was able to organize, acquire, and process up to 5,000,000 $km^2$ of images every day from the five-band multispectral imager (RGB, Red Edge, and NIR bands), with 6.5 m GSD to generate land information products [41]. In 2013, SkyBox, with its micro-satellite SkySat-1, provided 0.9 m resolution images in Panchromatic filters and became the first company ever to capture and release HD videos acquired in space [42]. The resolution of the SkySat satellite images and videos is high enough to observe objects that impact the global economy, such as terrain, vehicles, and shipping containers [43].

Concurrently to the progress of SmallSats and the widespread of constellations, the turn of the XXI century also represented a milestone for a particular class of "very" small satellites, i.e., the CubeSats. CubeSats were born as a collaborative project between Robert J. Twiggs at Stanford University's Space Systems Development Laboratory (SSDL) and Prof. Jordi Puig-Suari at California Polytechnic State University (Cal Poly) [44]. The idea was to rapidly develop a pico-satellite that could give university students accessibility to space for conducting scientific experiments and testing out new technologies [45–47]. Indeed, the standardized design and compact dimensions allowed to reduce both costs and developing time, as well as to use the same type of deployment system (Poly-PicoSatellite Orbital Deployed (P-POD)), which provides a verified and reliable procedure, preventing any potential challenges in the phase of launch as a secondary payload [48,49]. These characteristics, together with the advancement in the miniaturizing technology, have made CubeSats the key element in the space industry, not only for the EO [50–52], but also for the exploration of our solar system [53–55].

### *2.2. Current Status of Small Satellite Payload for Earth Observation*

Small satellites for EO often carry optical or microwave sensors, providing observations with a range of spatial, spectral, and temporal resolutions. Here, we will briefly provide an overview of these sensors (values are taken from manufacturer or space agency websites).

In Table 2, we list a number of small satellites (still active or ended), equipped with either remote sensing optical or microwave payloads. These examples have been developed during the last few decades for the EO, with characteristics (e.g., payload characteristics, revisiting time, and costs) that can be fully or partially suitable to image and monitor the study cases presented in this work. In Table S1 in the Supplementary Material, we reported the same parameters, but for medium to large satellites, as comparison.

**Table 2.** List of the small satellites used in the text, with their main characteristics.

| Satellite Acronym | Satellite Name | Satellite Class | Satellite Description and Main Goals | Satellite Weight (kg) | Satellite Size | Orbit Altitude (km) | Payload | Telescope or Antenna Aperture Diameter (mm) | f/Number Focal Length | FoV/ Beamwidth | Spatial Ground Resolution (m) | SNR | Swath Width | Spectral Range (μm) * /Frequency | Spectral Resolution | Polarimetric Capabilities | Revisiting Time | Constellation | Year * | Company (Country) | References |
|---|---|---|---|---|---|---|---|---|---|---|---|---|---|---|---|---|---|---|---|---|---|
| Capella X-SAR | | Micro | • Earth's monitoring to provide the most frequent, timely, and high-quality SAR imagery products available, accessible through an intuitive self-serve online platform | <40 | - | 485–525 sun-synch | *X-SAR*/3 acquisition modes: *SL*: spotlight, *SP*: sliding spotlight, *SM*: StripMap | 8 $m^2$ once deployed | - | - | SL: 0.5–0.7 m SP: 0.8–1.2 m SM: 1.6–2.4 m | SL: −14 to −10 dB SP: −17 to −14 dB SM: −20 to −16 dB | SL: 5 km × 5 km SP: 5 km × 10 km SM: 5 km × 20 km | X-band: 9.4–9.9 GHz | bandwidth of up to 500 MHz | yes: S (HH) | <1 week | Cappella is born as a constellation of 36 microsatellites | 2018 | Capella Space Company (USA) | [43,56–58] |
| DubaiSat-2 | | Mini | • Technologically advanced follow-up of the DubaiSat-1 • Electro-optical imagery for the EO, with very high spatial resolutions | ≤300 | 1.95 (height) × 1.5 m (diameter) | 600 sun-synch | *HiRAIS* (High Resolution Advanced Imaging System) | 420 mm | 5.7 m | - | <1 m PAN, <4 m MS @ 600 km altitude | - | 12 km @ nadir | PAN: 550–900 nm MS1-Blue: 450–520 nm MS2-Green: 520–590 nm MS3-Red: 630–690 nm MS4-NIR: 770–890 nm | - | no | <8 days | PanGeo constellation (9 satellites) in 2014 DubaiSat-2 worked in conjunction with Deimos-2 | 2013 (>5 years) | MBRSC/ SI (Dubai, Korea) | [43,56] |
| Flock Imaging Constellation | | CubeSat | • Constellations operating in a continuous monitoring mode and nadir pointing, to capture imagery of the sunlit portion of the Earth's surface • Rapid iterative design and frequent replacement and testing in space of nanosatellites, to continuously deploy improved S/C and P/L into two types of orbits | 5 | 3U | 370–475 (ISS orbit or sun-synch orbit) | *Planet Scope/PS* (3 generations of optical systems, PS0, PS1, PS2) | 90 | - | *PS2*: HFOV: 21.8 km VFOV: 14.5 km | 3–5 m @nadir (e.g., : PS2: 3.3 m @ ISS altitude) | - | 21.8 km | *PS2*: Red: 630–714 nm Green: 515–610 nm Blue: 424–478 nm NIR: 70–900 nm | < 90 nm | no | <1 day | Constellation of initially 28 nano satellites: constellation replenished over time | 2014 (1 year per satellite in ISS orbit, or 2–3 years per satellite in sun-synch orbit) | Planet Labs (USA) | [43,56,59] |
| HARP | Hyper-Angular Rainbow Polarimeter | CubeSat | • Precursor for the new generation of imaging polarimeters • Measure the microphysical properties of aerosol, cloud water, and ice particles in the atmosphere | 6 | 3U | 400 | *Imaging Polarimeter* | - | - | 94° cross-track 113° along-track | 2.5 km | - | ≥900 km | 440, 550, 670, 870 nm | - | yes | - | no | 2019 (>1 year) | NASA/ ESTO (USA) | [43,56] |
| ICEYE | | Micro | • Timely and reliable Earth's observation data • Goal of enabling better decision making | 85 | 70 cm × 60 cm | 560–700 sun-synch and ECT | *X-SAR*/3 acquisition modes: *SM*: strip mode, *SP*: spot mode, *SC*: scan mode | 3.2 m (along-track) × 0.4 m | - | - | ST: 3 m SP: 1 m SC: <15 m | ST: −22 to −21.5 dB SP: −18 to −15 dB SM: −22.2 to −21.5 dB | ST: 30 × 50 km SP: 5 × 5 km SC: 100 × 100 km | X-band: 9.65 GHz | bandwidth: 37.6–299 MHz | yes: S (VV) | 20 h mean revisit time at equator | 18 microsatellites | 2018 | ICEYE Ltd. of Espoo (Finland) | [43,56,57,60] |
| JASON–1 | | Mini | • Monitoring the global ocean circulation and events such as El Nino • Understanding the ocean–atmosphere relation • Improving the global climate predictions | 500 | 954 mm × 954 mm × 1000 mm | 1324 drift | *Poseidon-2* (altimeter) *JMR* (microwave radiometer) *DORIS* (Doppler Orbitography and Radiopositioning) *BlackJack* (GPS flight receiver) | *Poseidon-2*: 1.2 m | - | *JMR*: beamwidth = 1.2° @ 18.7 GHz, 1.0° @ 23 GHz, 0.7° @ 34 GHz | - | *Poseidon-2*: Ku-band: 3.2 dB C-band: 0.9 dB | - | *Poseidon-2*: Ku-band, C-band *JMR*: 23.8 GHz, 34 GHz, 18.7 GHz | - | no | 9.9 days | Jason-1 works in conjunction with TOPEX/ Poseidon and Jason-2 | 2001–2013 | CNES/ NASA (France, USA) | [43,56] |

**Table 2.** *Cont.*

| Satellite Acronym | Satellite Name | Satellite Class | Satellite Description and Main Goals | Satellite Weight (kg) | Satellite Size | Orbit Altitude (km) | Payload | Telescope or Antenna Aperture Diameter (mm) | f/Number Focal Length | FoV/ Beamwidth | Spatial Ground Resolution (m) | SNR | Swath Width | Spectral Range (μm) * /Frequency | Spectral Resolution | Polarimetric Capabilities | Revisiting Time | Constellation | Year * | Company (Country) | References |
|---|---|---|---|---|---|---|---|---|---|---|---|---|---|---|---|---|---|---|---|---|---|
| OSTM/ JASON-2 | Ocean Surface Topography Mission/ JASON-2 | Mini | • Extending the time series of ocean surface topography measurements to:<br>(a) obtain a continuous record of observations<br>(b) determine the variability of ocean circulation at decadal time scales from combined data record with T/P and Jason<br>(c) improve the measure of the time-averaged ocean circulation<br>(d) improve the measure of global sea-level change<br>(e) improve open ocean tide models | 553 | 1 m × 1 m × 3.7 m | 1336 drift | *Poseidon-3* (solid-state radar altimeter) *AMR* (Advanced Microwave Radiometer) *DORIS* (Doppler Orbitography and Radiopositioning Integrated by Satellite) *TRSR-2/GPSP* (Turbo Rogue Space Receiver-2) *LRA* (Laser Retroreflector Array) | *Poseidon-3:* 1.2 m | - | *Poseidon-3:* 1.28° (Ku-band), 3.4° (C-band) | - | *Poseidon-3:* 3.2 dB (Ku-band), 0.9 dB (C-band) | - | *Poseidon-3:* C-band: 5.3 GHz Ku-ban: (13.575 GHz | *Poseidon-3:* 320 MHz bandwidth | no | 10 days | Jason-2 works in conjunction with TOPEX/ Poseidon and Jason-1 | 2008–2019 | NOAA/ EUMETSAT (USA/ Europe) | [43,56,61] |
| JASON-3 | | Mini | • Providing continuity to the unique accuracy and coverage of the TOPEX/Poseidon, Jason-1, and OSTM/Jason-2 missions in support of operational applications related to extreme weather events and operational oceanography and climate applications and forecasting | 553 | 1 m × 1 m × 3.7 m | 1336 drift | *Poseidon-3B* (altimeter) *AMR-2* (Advanced Microwave Radiometer) *DORIS* (Doppler Orbitography and Radiopositioning Integrated by Satellite) *LRA* (Laser Retroreflector Array) *GPSP* (Global Positioning System Payload) | *Poseidon-3B*: 1.2 m | - | *Poseidon-3B:* 1.28° (Ku-band), 3.4° (C-band) | - | *Poseidon-3B:* 3.2 dB (Ku-band), 0.9 dB (C-band) | - | *Poseidon-3B:* C-band: 5.3 GHz Ku-band: 13.575 GHz *AMR:* 18.7, 23.8 and 34 GHz | *Poseidon-3B:* 320 MHz bandwidth | no | 9.9 days | Jason-3 works in conjunction with Jason-1 and Jason-2; it belongs to the NOAA/ EUMETSAT/ CNES/NASA program for monitoring weather, climate, and the environment | 2016 | NOAA/ EUMETSAT/ CNES/ NASA (USA/ Europe) | [43,56,62] |
| N2 | Nigeria Sat-2 | Mini | • Supporting food supply security, agricultural, and geology applications<br>• Supporting mapping and security applications<br>• Supporting development of the national GIS infrastructure<br>• Providing continuity and compatibility with the existing NigeriaSat-1 system | 270 | - | 700 × 733 km sun-synch | *VHRI* (Very High-Resolution Imager) *MRI* (medium resolution imager) | *VHRI:* 385 | - | - | *VHRI:* PAN: 2.5 m MS: 5 m *MRI:* 32 m | - | *VHRI:* 20 km for 2.5 m & 5 m GSD *MRI:* 300 km for 32 m GSD | *VHRI:* PAN: 450–900 nm Blue: 450–520 nm Green: 520–600 nm Red: 630–690 nm NIR: 760–900 nm *MRI:* 4 spectral bands | *VHRI:* > 140 nm | no | 2 days | DMC-1G constellation | 2011–2018 | NASRDA/ SSTL (Nigeria, UK) | [43,56] |
| NX | Nigeria-Sat-X | Micro | • Training model to give the NASRDA engineers the Know-How Technology experience in the satellite specifications, project management, system engineering, manufacturing, testing, assembly, and final system testing of a spacecraft | 87 | 0.6 m × 0.6 m × 0.6 m | 663 km × 700 km sun-synch | *SLIM6* (Surrey Linear Imager Multispectral 6 channels, but 3 spectral bands) | - | - | 26.6° | 22 m @ nadir | >100 | >600 km (>300 km per channel) | Green: 520–620 nm Red: 630–690 nm NIR: 760–900 nm | <900 nm | no | 3–5 days | DMC-2G constellation | 2011 (5 years) | NASRDA/ SSTL (Nigeria, UK) | [43,56] |

**Table 2.** *Cont.*

| Satellite Acronym | Satellite Name | Satellite Class | Satellite Description and Main Goals | Satellite Weight (kg) | Satellite Size | Orbit Altitude (km) | Payload | Telescope or Antenna Aperture Diameter (mm) | f/Number Focal Length | FoV/ Beamwidth | Spatial Ground Resolution (m) | SNR | Swath Width | Spectral Range (µm) * /Frequency | Spectral Resolution | Polarimetric Capabilities | Revisiting Time | Constellation | Year * | Company (Country) | References |
|---|---|---|---|---|---|---|---|---|---|---|---|---|---|---|---|---|---|---|---|---|---|
| Nova-SAR-1 | | Mini | • Making SAR observation missions more affordable to a customer base<br>• Opening up new application-oriented options in the microwave region of the spectrum | 450 | - | 580 sun-synch | *S-SAR*/4 acquisition modes: *SS*: ScanSAR mode, *MS*: maritime surveillance mode, *SM*: StripMap, *WS*: ScanSAR Wide | $3\times1$ m$^2$ | - | - | SS: 20 m<br>MS: 30 m<br>SM: 6 m<br>WS: 30 m | SS:<br>< −18 dB<br>MS:<br>< −12 dB<br>SM:<br>< −18.5 dB<br>WS:<br>< −19 dB | SS:<br>50–100 km<br>MS: 750 km<br>SM:<br>13–20 km<br>WS:<br>55–140 km | S-band | - | yes: S, D, T (HH, VV, HV, VH) | Polar orbit: 0.9–4.4 days<br>equatorial orbit: 0.5–1.3 days<br>constellation: < 8 h | yes<br>3 satellites | 2018<br>(7 years) | SSTL/ UKSA (UK) | [43,56,57,63] |
| PARASOL | Polarization and Anisotropy of Reflectances for Atmospheric Science coupled with Observations from a Lidar | Micro | • Monitoring Earth's atmosphere<br>• Understanding the role of clouds and aerosols in climate mechanisms (What effect does global warming have on cloud cover? How do clouds and aerosols interact?) | 120 | 60 cm × 60 cm × 80 cm | 705 sun-synch | *POLDER-3* (radiometer/ polarimeter | - | - | ±43° to ±57° | 6 km × 7 km at nadir | 200 | 2400 km | 9 wavelengths, with 3 polarizations at 3 wavelengths in the 443–1020 nm range:<br>443.5 ± 6.7 nm<br>490.9 ± 8.2 nm<br>563.8 ± 7.7 nm<br>669.9 ± 75.6 nm<br>762.9 ± 5.5 nm<br>762.7 ± 19.1 nm<br>863.7 ± 16.9 nm<br>907.1 ± 10.6 nm<br>1019.6 ± 8.6 nm | - | yes: T | 2 days | A-train constellation | 2004–2013 | CNES (France) | [43,56,64] |
| PICASSO | Pico-Satellite for Atmospheric and Space Science Observations | Pico | • Demonstrating the potentiality of tiny satellites to achieve a very high ratio of "science data versus cost"<br>• Determining the ozone distribution in the stratosphere, the temperature profile up to the mesosphere, and the electronic plasma characterization in the ionosphere | 3.8 | 3U | 530 | *VISION* (Visible Spectral Imager for Occultation and Nightglow)<br>*SLP* (sweeping Langmuir probe) | - | - | *VISION:* 2.5° | vertical res = 2 km | - | - | *VISION:* 430–800 nm | FWHM <10 nm | no | 2–3 weeks | no | 2020 (29 months) | BISA, VTT, Clyde Space (Belgium, Finland, UK) | [43,56] |
| RainCube | Radar in a CubeSat | CubeSat | • Observing the short-time evolution of weather processes, which is necessary to validate and improve the current assumptions and skills of numerical weather models | 5.5 | 6U | 400 | *miniKaAR-C* (miniaturized Ka-band Atmospheric Radar for CubeSats)<br>*KaRPDA* (Ka-band radar parabolic deployable antenna) | *KaRPDA:* 0.5 m deployable | - | - | Horizontal: 7.9 km<br>Vertical: 120 m | - | - | Ka-Band: 35.75 GHz | - | no | - | yes | 2018–2020 | NASA ESTO (USA) | [43,56,65] |
| RapidEye | | Micro | • Land information services (agriculture, environment, forestry, mapping, intelligence and defense, security and emergency, and visual simulation) to a variety of customers | 156 | 0.78 m × 0.938 m × 1.17 m | 620 sun-synch | *MSI* (Multi-Spectral Imager) | 145 mm | f/4.3<br>633 mm | ± 6.75° @ nadir | 6.5 m @ nadir | 50–250 | > 70 km @ 620 km altitude | 5 bands in the 400–850 nm range:<br>440–510 nm<br>520–590 nm<br>630–685 nm<br>690–730 nm<br>760–850 nm | - | no | < 1 day @ off-nadir<br>5.5 days @ nadir | 5 satellites | 2008–2020 | RapidEye AG (Germany) then acquired in 2015 by Planet Labs (USA) | [43,56,63,66] |

**Table 2.** *Cont.*

| Satellite Acronym | Satellite Name | Satellite Class | Satellite Description and Main Goals | Satellite Weight (kg) | Satellite Size | Orbit Altitude (km) | Payload | Telescope or Antenna Aperture Diameter (mm) | f/Number Focal Length | FoV/ Beamwidth | Spatial Ground Resolution (m) | SNR | Swath Width | Spectral Range (μm) * /Frequency | Spectral Resolution | Polarimetric Capabilities | Revisiting Time | Constellation | Year * | Company (Country) | References |
|---|---|---|---|---|---|---|---|---|---|---|---|---|---|---|---|---|---|---|---|---|---|
| RAVAN | Radiometer Assessment usingVertically Aligned Nanotubes | CubeSat | • Demonstrating technology: compact and low cost satellites can be used to collect key measurements to predict changes in Earth's climate | <5 | 3U | 617 syn synch | 4 RAVAN radiometers: *2 VACNT* (vertically aligned carbon nanotube) adsorbers + 2 *black-painted cavity* absorbers | - | - | 130° | - | - | - | *PTOT Primary* / *(VACNT) Total channel:* UV–far IR *PSW Primary* / *(VACNT) SW channel:* UV–5.5 m *STOT Secondary* / *(cavity) Total channel:* UV–far IR *SSW Secondary* / *(cavity) SW channel:* UV–5.5 m | - | no | ≤ 3 days | No technology demonstration for the ERB constellation | 2016 (20 months) | NASA's ESTO (USA) | [43,56] |
| SeaHawk-1 | | CubeSat | • Demonstrating the potential scientific applications of a high resolution (~120m) ocean color instrument placed on 3U CubeSat Platforms | 5 | 3U | 575 | *HawkEye Ocean Color Sensor* | - | - | ± 11.3° | 120 m | 150–490 | 250 × 400 km | 8 SeaWiFS bands: 412 nm, 443 nm, 490 nm, 510 nm, 555 nm, 670 nm, 750.9 nm, 865 nm | 14.7–40 nm | no | 9 days | Socon Constellation | 2018 (18–24 months) | UNCW (USA) | [43,56] |
| SkySat constellation | Generation A: SkySat-1 Generation B: SkySat-2 Generation C: SkySat-3 to 21 | Micro | • Constellation of high-resolution and frequent Earth imaging satellites • Addressing two distinct markets: (a) various environmental applications (e.g., monitoring agriculture, forestry, and other natural resources) (b) asset tracking, where S/C images help customers monitoring various facilities for changes | G-A: 83G-C: 110 | *G-A:* 60 cm × 60 cm × 80 cm *G-C:* 60 cm × 60 cm × 95 cm | *Skysat 1–2:* 600 km, sun-synch *Skysat 3–15:* 500 km at launch, lowered to 450 km in early 2020, sun-synch *Skysat 16–18:* 400 km inclined, non-sun-synch | *SkySat camera:* mono- and stereo-imaging, and video acquisition modes | *SkySat-C:* 350 mm | f/10.3 3.6 m | 2.0 km × 1.1 km | *SkySat-1–2:* PAN: 0.86 m MS: 1 m *SkySat-3–15:* PAN: 0.65 m MS: 0.81 m *SkySat-16–21:* PAN: 0.57 m MS: 0.75 m | - | *SkySat-1–2:* 8 km *SkySat-3–15:* 5.9 km *SkySat-16–21:* 5.5 km | PAN: 450–900 nm Blue: 450–515 nm Green: 515–595 nm Red: 605–695 nm NIR: 740–900 nm | - | no | *Constellation:* sub-daily, 6–7 times at worldwide average, 12 times max *Satellites:* 4–5 days (reference altitude: 500 km) | Constellation replenished over time (21 satellites in 2021) | 2013 (>4–6 years) | Skybox Imaging, then renamed as Terra Bella in 2016 (USA) | [43,56] |
| TecSAR | SAR Technology Demonstration Satellite | Mini | • Technology demonstration mission for military purposes • Providing high-resolution SAR imagery, day and night, in all weather conditions, at an affordable cost | 260 | - | 403 km × 581 km | *X-SAR* (X-band Synthetic Aperture Radar)/4 acquisition modes: *WS*: wide coverage ScanSAR, *SM*: StripMap, *SS*: Super StripMap, *SL:* spotlight | 3 m | - | - | WS: 8m SM: 3 m SS: 1.8 m SL: <1 m | >200 | <100 km | X band: 9.59 GHz | - | yes: HH, HV, VH, VV | 3–4 days | no | 2008 (>5 years) | Israel's MoD (Israel) | [43,56,57] |
| TEMPEST-D | Temporal Experiment for Storms and Tropical Systems Technology—Demonstration | CubeSat | • Validating the performance of a 6U CubeSat microwave radiometer designed to study precipitation events on a global scale • Observing the time evolution of clouds and studying the conditions that control the transition from non-precipitating to precipitating clouds using high-temporal resolution observations | 3.8 | 6U | 410 | *MM Radiometer* (millimeter-wave radiometer) | - | - | - | from 12.5 km @ 181 GHz to 25 km @ 87 GHz | NEΔT: 0.20 K @ 89 GHz 0.35 K @ 165 GHz 0.55 K @ 176 GHz 0.55 K @ 180 GHz 0.75 K @ 182 GHz | 825 km | 5 frequencies: 89 GHz, 165 GHz, 176 GHz, 180 GHz, and 182 GHz | bandwidth requirements: 4 ± 1 GHz @ center frequencies of 89 and 165 GHz 2 ± 0.5 GHz @ 176, 180, and 182 GHz center frequencies | yes: Quasi-H or Quasi-V Pol | 3–5 min for up to 30 min | Demonstrative CubeSat for the future TEMPEST constellation | 2018 (90 days after on-orbit commissioning) | Colorado State University/NASA (USA) | [43,56,67] |

**Table 2.** *Cont.*

| Satellite Acronym | Satellite Name | Satellite Class | Satellite Description and Main Goals | Satellite Weight (kg) | Satellite Size | Orbit Altitude (km) | Payload | Telescope or Antenna Aperture Diameter (mm) | f/Number Focal Length | FoV/ Beamwidth | Spatial Ground Resolution (m) | SNR | Swath Width | Spectral Range (µm) * /Frequency | Spectral Resolution | Polarimetric Capabilities | Revisiting Time | Constellation | Year * | Company (Country) | References |
|---|---|---|---|---|---|---|---|---|---|---|---|---|---|---|---|---|---|---|---|---|---|
| TROPICS | Time-Resolved Observations of Precipitation structure and storm Intensity with a Constellation of SmallSats | CubeSat | • Studying the development of tropical cyclones through rapid-revisit sampling<br>• Relating the precipitation structure evolution, including the diurnal cycle, to the evolution of the upper-level warm core and associated intensity changes<br>• Relating the occurrence of intense precipitation cores (convective bursts) to storm intensity evolution<br>• Relating the retrieved environmental moisture measurements to coincident measures of storm structure (including size) and intensity<br>• Assimilating microwave radiances and/or retrievals in mesoscale and global numerical weather prediction models to assess impacts on storm track and intensity | 6 | 3U | 600 (550 ± 50 km tolerance) sun-synch | *TROPICS radiometer:*<br>W-band:<br>92 GHz<br>F-band<br>(7 channels):<br>114–119 GHz<br>G-band<br>(4 channels):<br>183–204 GHz | - | - | - | *W-band (90GHz):*<br>29.6 km @ nadir, 50.7 km @ EAS<br>(Effective Across Scan)<br>*F-band (118 GHz):*<br>24.1 km @ nadir, 41.2 km @ EAS<br>*G-band (183 GHz):*<br>16.1 km @ nadir, 27.5 @ EAS<br>*G-band (205 GHz):*<br>15.2 km @ nadir, 26.0 @ EAS | NEΔT:<br>2.0 K @ 90 GHz<br>1.5 K @ ~110–120 GHz<br>1.0 K @ ~180–200 GHz | 2000 km | Ch1: 91.655 GHz<br>Ch2: 114.50 GHz<br>Ch3: 115.95 GHz<br>Ch4: 116.65 GHz<br>Ch5: 117.25 GHz<br>Ch6: 117.80 GHz<br>Ch7: 118.24 GHz<br>Ch8: 118.58 GHz<br>Ch9: 184.41 GHz<br>Ch10: 186.51 GHz<br>Ch11: 190.31 GHz<br>Ch12: 204.80 GHz | bandwidth: ~300–2000 MHz | no | 30 min | 6 satellites TROPICS | 2021<br>(9 years):<br>Pathfinder 2022<br>(9 Years):<br>Constellation | MIT/ Lincoln Labs, NASA (USA) | [43,56] |
| ZACUBE-2 | | CubeSat | • Technological demonstration: automatic identification system (AIS) receiver to test AIS message reception using its SDR-based payload<br>• Earth's observation with a near-infrared imager for forest fire detection and ocean color | 4 | 3U | 480 km × 508 km | *K-line camera*<br>(medium resolution CMOS imager)<br>*VHF AIS/VDE receiver* | - | - | *K-line camera:*<br>7.8° × 6.2° | *K-line camera:*<br>53 m | - | *K-line camera:*<br>68 km | *K-line camera:*<br>770 nm | *K-line camera:*<br>1 nm bandwidth<br>*VHF AIS/VDE:*<br>extended VDES bands from 156.75 MHz to 162.05 MHz | *VHF AIS/VDE:*<br>yes<br>(linear) | - | Yes:<br>MDASat-1 constellation | 2018 | Cape Peninsula University of Technology (South Africa) | [43,56] |

* The years of the missions are given as an interval when it is a past mission. When only one date is given, this refers to the launch date. The eventual numbers in brackets refer to the expected lifetime, as given in the references.

#### 2.2.1. Optical Payloads

The performance of an optical payload, in terms of spatial and signal-to-noise ratio (SNR), is limited by aperture size. Remote optical sensing systems mounted on small satellites usually employ aperture diameters $\leq$400 mm (cf. Table 2) (e.g., [68]), allowing for a spatial resolution ranging from 1 to 4 m, which is limited by light diffraction and dependent on satellite altitude. New methods have been implemented to limit sensors' volume and mass with similar resolutions to larger satellites, e.g., the high-precision telescope (HPT), a high spatial resolution multispectral sensor sized for small platforms [69], and the deployable optical systems [24].

At the same time, small satellites provide a unique opportunity for launching affordable constellations, which can provide daily return cycles. In this respect, small satellites reach the temporal resolutions that are not practical with large satellites. Constellations such as SkySat (Terra Bella), Flock Imaging Constellation and RapidEye (Planet Labs), ICEYE (ICEYE Ltd. of Espoo), NovaSar, and Disaster Monitoring Constellation Second Generation (SSTL/UKSA) are examples of small satellites working cooperatively to provide a daily coverage of the terrestrial surface (cf. Table 2).

#### 2.2.2. Microwave Payloads

Earth imaging in the microwave range is mainly achieved using the synthetic aperture radar (SAR) technology, which synthesizes the elevation by processing a tailored signal (e.g., [57,70]). This technology allows to increase the spatial resolution using a smaller antenna than in the real aperture radar (RAR) system. Due to its day, night, and (almost) all-weather capabilities, SAR is a key tool for a broad range of EO applications, including the observation of oceans (currents, winds, waves, pollution, etc.), the cryosphere (coverage and extension of ice and snow, navigation routes, etc.), and lands (coverage and extension of vegetation, evolution of geological and tectonic structures, utilization of terrains for agriculture, etc.) [57,71–73].

The SAR system was the main payload of large satellites such as Sentinel-1 (ESA) and TSX (BMBF, DLR), medium-large satellites such as COSMO-SkyMed (first and second generations, ASI) (cf. Table S1 in the Supplementary Materials), down to the smaller sizes (<500 kg) such as TecSAR (Israe's MoD) and NovaSAR-1 (SSTL/UKSA) (cf. Table 2). Similar to small satellites with optical payloads, constellations of SAR-carrying satellites can improve observation revisiting time (e.g., ICEYE (ICEYE Ltd. of Espoo), cf. Table 2).

Passive instruments operating in the microwave range are termed as microwave radiometers (MWRs). They collect microwave radiation naturally emitted by the Earth, guaranteeing continuous, large-scale, all-day, and almost all-weather Earth Observations, which are of paramount importance for environmental monitoring, for instance soil moisture and sea surface salinity [74,75].

MWRs can be built by means of the "aperture synthesis" approach too [76], allowing spatial resolutions that otherwise would require the use of antennas with a larger aperture [77]. Synthetic aperture microwave radiometers (SA-MWRs) are based on the cross-correlation of signals collected by different pairs of antennas, placed at varying antenna-pair spacings [76]. Such baselines represent the visibility function in the frequency domain, which must then be transposed into the brightness temperature map in the spatial domain through an inversion algorithm (e.g., Fourier transform) [78].

MWRs can be designed to allow measurements at a given combination of frequency and polarization (single-channel MWRs), such as the Soil Moisture Active Passive (SMAP) radiometer and the Microwave Imaging Radiometer using Aperture Synthesis (MIRAS), which is part of the European Space Agency (ESA) Soil Moisture and Ocean Salinity (SMOS) mission, or they can call for multi-frequency and multi-polarization capabilities (multi-channel MWRs). The latter category includes instruments that can perform measurements at different channels (i.e., using different frequency/polarization combinations), e.g., (i) the Special Sensor Microwave Imager (SSM/I), which covers four frequencies (ranging from 19.35 GHz to 85.5 GHz) and seven channels (i.e., all the frequency channels, with the

exception of the 23.235 GHz one, allow for collecting measurements at both vertical and horizontal polarizations); (ii) the Special Sensor Microwave Imager Sounder (SSMIS), which is a 24-channel, microwave radiometer with channel frequencies ranging from 19 GHz to 183 GHz; (iii) the 12-channel Advanced Microwave Scanning Radiometer 2 (AMSR2); and (iv) the 10-channel Microwave Radiation Imager (MWRI) [79]. Although MWRs are mesoscale sensors, a number of products have been also proposed to retrieve parameters on a regional scale [79–81].

### *2.3. CubeSats for Earth Observation as an Endpoint Case of Small Satellites*

CubeSats are a class of research spacecraft that are classified in the borderline between nano- and pico-satellites. The original CubeSat is a 10-cm cube, less than 1.33 kg in weight [82], but this standard shape, the so-called 1U factor form, can be typically extended to 2U and 3U ones, and up to 27U [83]. CubeSats have recently sprung into the spatial marketplace to address targeted science questions in a rapid and affordable manner (e.g., [57,84]). The advantages given by lower costs, fast development, and the possibility of launching several dozen CubeSats by means of a single rocket, have brought forth the potential for radically new mission architectures. These consist in very large constellations of CubeSats, which allow to combine the temporal resolution of GEO missions with the spatial resolution of LEO missions, thus breaking a traditional trade-off in EO mission design (e.g., [15,85]). Several EO measurements, such as natural-disaster and water-resource monitoring [86], could potentially be compatible with the current state-of-the-art CubeSat technology, even if some of them have never been addressed by any mission of this class [52].

### *2.4. DORA: Deployable Optics for Remote Sensing Applications*

The development of small satellites highlighted how EO through remote sensing relies on the compromise between the necessity of high spatial, spectral, and temporal resolutions, payload miniaturization, and the availability of resources from space agencies and companies for the space program. The data acquired in the spectral range from VIS to MW suffer particularly from the smaller size of the telescope or antenna. The limited size and weight resources, mandatory for small satellites, implies a small primary mirror, and/or a lower length of the telescope assembly, reducing its performance in terms of spatial resolution and SNR. Large satellites can indeed host sensors as large as 500–600 mm in diameter, whereas small satellites can accommodate sensors with diameters as large as 300–400 mm (cf. Table 2 and Table S1 in the Supplementary Material). The lower area of the collector represents the troublesome challenge for having data at a high resolution. Remote sensing payloads operating in the MW suffer as well because of the antenna's size and the platform's altitude (the higher the platform altitude, the larger the antenna needs to be to obtain a reasonable spatial resolution).

The new design concept, based on a deployable approach (e.g., [24]), represents a viable architecture to accomplish scientific objectives and applications that are otherwise difficult to reach by small satellites. The deployable technology allows both minimization of the payload volume during the launch and the cruise to the final orbit, and good performances, similar to those of the instruments mounted in larger platforms, during the period of activity. Precision-deployable, stable, optical telescopes, which can fit inside small and low-cost launch vehicles, are prime examples of a technology that will yield breakthrough benefits for future scientific and commercially-oriented applications (e.g., [87]). Similarly, SAR technology synthesizes the flying altitude through a tailored signal processing, allowing to increase the spatial resolution using an antenna much smaller than the physical antenna used in an RAR system [70].

The Italian Ministry of Research funded the "Deployable Optics for Remote sensing Applications" (DORA) project in the framework of the Italian National Research Plan 2015–2020, which will be active until April 2022. DORA is a partnership between private companies (led by SITAEL, the largest Italian private company operating in the space

sector), research institutes (INAF—Institute for Space Astrophysics and Planetology (Rome) and INAF—Astronomical Observatory of Padua), and academic centers (University of Naples "Parthenope" and Politecnico of Milan) (e.g., [87]). The objective of the project is to design, realize, and test a prototype of a deployable optical system for remote sensing applications in the VIS to TIR spectral range, and a planned application in the MW spectral range. A deployable telescope and a straylight shield will be interfaced to a focal plane instrument, which can include either a camera or a Fourier spectrometer. The telescope, kept in a closed configuration during the launch to minimize the volume, is then fully deployed by means of actuators in its operative configuration once in flight. A similar deployable system could be eventually modified for extending the antennas used for microwave instrumentations (e.g., [65,88]).

The DORA system has been realized as a prototype for the next generation of space instruments for EO. It has, therefore, been designed to satisfy the requirements of a selection of applications in the ecological and environmental fields, which would best take advantage of deployable instrumentations. These applications will be presented and discussed in the following Section 3, to highlight the efficiency of the deployable systems, and to discuss more generally the efficiency of small space platforms for remote sensing acquisitions. The heterogeneity of the topics and areas examined in these applications, which are used as guidelines to define the instrument requirements, will ensure that the DORA prototype has suitable performances not only for these specific study cases, but also for a broader spectrum of future applications.

## 3. Study Cases

In this section, we present an overview of possible applications that would benefit from remote sensing data, in particular in the new perspective provided by small satellites. The applications discussed in this paper cover highly dynamic processes in the environments ranging from mid-latitude to polar seas and atmospheres. See Table 2 and Table S1 in the Supplementary Material for details about the small and large satellites, respectively, mentioned in this section.

### *3.1. Application 1: Composition of the Atmosphere*

The Earth's atmosphere composition is primarily $N_2$, $O_2$, Ar, and $H_2O$, plus trace gases (in the order of ppm) (e.g., [89]). Despite their negligible amount, these trace molecules represent a key factor in controlling the radiation budget of the Earth. Compounds such as $H_2O$, $CO_2$, $CH_4$, $O_3$, $N_2O$, $SO_2$, and halocarbons are examples of greenhouse gases, which, trapping the incident solar radiation, determine the degree of heating at the Earth surface, and at the end influence the climate (e.g., [89,90]).

The effects of anthropogenic gases on the atmosphere can be evaluated by monitoring: (i) the ozone loss in the lower stratosphere, (ii) the source of the polluting gases, and (iii) how these gases are transported vertically and horizontally through the atmosphere [89]. For instance, the mapping of $SO_2$, which can have either a natural (e.g., from volcanic eruptions, [91]) or anthropogenic (e.g., air traffic and industrial processes, [92]) origin, is important, as it contributes to aerosols formation, which cause variations in the total radiative balance and in the air navigation visibility when injected in large quantities into the atmosphere [93]. At a spatial resolution <1 km, it would be possible to monitor $SO_2$ in volcanic plumes and from air and maritime navigation, through their emission trails.

Spectrometers, operating from the near UV up to TIR, are used to study the atmospheric composition, e.g., the main IR absorption lines are associated with vibro-rotational transitions of trace gases [94], and concentration, by iterative inverse methods (c.f., [94–96]). As reported in [97,98], differential absorption spectroscopy is commonly adopted to detect and quantify the narrow absorption lines in the UV–VIS spectral range characteristics of a specific trace gas. Micro- and nano-satellites have taken a leading role in the atmospheric characterization (e.g., HARP [99], PARASOL [100], and PICASSO [101]), coming up beside and replacing the large satellites (e.g., satellites such as ESA Sentinel-5P [102,103],

NASA/Aura [104], or programs such as EUMESAT MetOp [105,106], or fleets such as the NOAA's Joint Polar Satellite System (JPSS) [107,108]).

$SO_2$ can be monitored by micro- and nano-satellites equipped with innovative interferometers, such as the Fabry–Pérot interferometer (FPI) [97,98]. FPI technologies have been developed and applied, from UV to TIR, to micro-spectrometers placed in CubeSat-type hyperspectral imagers [109,110]. An operational version is aboard a CubeSat 2U form factor Nano satellite (a CubeSat multiple of the standard size 1U), which mounts a hyper-spectral infrared camera (0.9–1.4 μm). The FPI interferometer can also be realized by means of the Micro-electromechanical system (MEMS) technologies, which can determine the concentration of multiple gases at a nanometer resolution (e.g., [111–115]). To perform a global $SO_2$ coverage, e.g., to monitor volcanic emissions, the revisiting time should be at least 24 h. For regional/local acquisitions, e.g., to monitor aerial or naval routes, or industrial and urban plumes, the revisiting time should be few hours, which is feasible only by means of a constellation of satellites. The SNR for the FPI technique can be a factor of six to nine with respect to what can be obtained with the differential optical absorption spectroscopy [97].

### *3.2. Application 2: Polynya Monitoring in Polar Areas*

Polynyas are open water or very thin layers of sea ice (with a threshold of ice content varying between 0.5 and 0.7, e.g., [116,117]), which interpose the continuous ice blanket of the polar ice pack. They can be rectangular or oval shaped areas, reaching a size as large as 10 to $10^5$ $km^2$ (e.g., [118]). Polynyas are quasi-permanent and highly dynamic, evolving through occasional openings and closings at the same location for up to several months, and they can reform over many years [119–121]. They can be formed by the combined influence of geological features, e.g., seamount, upwelling of warm water into the upper ocean from the thermocline (induced by a large cyclonic ocean eddy and negative wind stress curl), and large-scale anomalous atmospheric warming [122]. Polynyas, due to their nature, play a key role in regulating heat, energy, mass, and momentum exchanges between the ocean and the atmosphere, because they are openings in an otherwise solid ice pack, which performs as a barrier to hinder heat flows and to prevent ocean evaporation [123].

The monitoring of polynya dynamics in the polar regions represents an important science quest. Occurring in polar, mostly inaccessible areas, polynyas can benefit from remote sensing observations. On one side, passive microwave radiometers, such as the Advance Microwave Scanning Radiometer AMSR-E onboard the NASA/Aqua EOS satellite, are one of the most useful instruments to cover large areas without being affected by light conditions and cloud presence, but they suffer from a very coarse resolution (6.5 to 25 km), which prevents disentangling sea ice and open water areas, as well as the thin ice thicknesses [124]. On the other side, satellite thermal infrared imagery (TIR), such as that acquired by the Moderate Resolution Imaging Spectroradiometer (MODIS) instrument on the Aqua EOS satellite, has better resolutions (down to 1 km) and wider swaths than microwave radiometers, but it has the drawback effect of being sensitive to the cloud coverage [125]. SAR and optical sensors represent an alternative for both a better spatial resolution (down to 10–150 m) and for the possibility to be mounted in small platforms. TecSAR and DubaiSat-2 are examples of small satellites equipped with an X-band SAR [126] and an optical system in the VIS to NIR range [127], respectively. In addition, working in the microwaves, SARs are independent from atmospheric perturbations. Because their revisiting times (days to weeks) and swaths are unsuitable for the long-term continuous monitoring of phenomena occurring in polynyas [128], only constellations of satellites are adequate for monitoring polynya dynamics (e.g., Cappella X-SAR [57], Flock imaging constellation [129], and RapidEye [130]).

Alternatively, the simultaneous use of complementary sensors (optical, thermal, and radar) has been thus suggested as the optimal approach for the long-term monitoring of polynyas, and/or the implementation of algorithms to strengthen the final output from the available data [124,131,132]. As, for instance, a multi-band TIR sensor, with at least two bands centered at about 11.0 μm and 12.0 μm, would be feasible to investigate polynyas [124,131].

Temperatures measured at different TIR provide the ice surface temperature (IST), i.e., the sea ice surface temperature, which is fundamental in monitoring the periods of ice blanket opening and closing and its production curve in the polar regions [133,134]. To determine IST value and polynya extent, a minimum revisiting time of 12 h, a swath of about 100 km, a minimum spatial resolution of about 500 m at nadir, and a noise-equivalent temperature difference (NE$\Delta$T) of 0.05 K, are required. This observation strategy would overcome the current space and time resolutions of the existing satellite performances that are limiting the monitoring of polynya.

Multispectral measurements, therefore, provide important characteristics of the polar oceans, e.g., the position of the marginal ice zone, presence and dynamics of icebergs, and eddies. Small satellites (eventually in a constellation configuration) represent the most convenient solution to study polynyas and improve the knowledge of their dynamics, allowing for a continuous monitoring of specific polar ocean areas at a very high resolution [135].

### *3.3. Application 3: Coastal Area Monitoring*

Coastal zones, i.e., sea areas within ~50 km from the mainland, are heavily affected by anthropogenic activities (e.g., [136–138]). Their continuous observation is thus crucial to formulate recovery plans, as well as the identification of new tools and methods to optimize both monitoring and management. Remote sensing in the spectral range from VIS to MW represents a key to monitoring the coastal zones [139]:

- *VIS*: 0.46 and 0.54 μm channels provide chlorophyll and other plankton pigment contents; the 0.7 to 0.8 μm region detects the presence of sediments and coastal areas pollution and/or erosion;
- *IR*: the ~1 to 5 μm range allows to clearly distinguish water from other surfaces;
- *TIR*: the 8 to 14 μm spectral range detects sea radiation emissions, allowing for the determination of the sea surficial temperature;
- *MW*: this spectral range provides sea roughness, which allows to obtain information on surface wind, and which affects emissivity, a quantity used to derive sea salinity once the sea surface temperature and the observational conditions are known.

Coastal oceanography is traditionally focused on measuring several geophysical variables, e.g., ocean color, surface temperature, salinity, sea surface height, and surface wind field. Coastal oceanography would benefit from synoptic observational strategies targeted at the ocean, both to monitor natural marine dynamics, and to track the evolution of anthropogenic phenomena (e.g., pollutant dispersion), in order to address any potential risk for the environment in a timely manner [140]. Combining different spectrum bands allows to: (i) distinguish the original ocean color, by limiting any atmospheric interference; and (ii) define the altimetry, by improving re-tracking techniques, taking into account coastal waveform characteristics [141–143]. In the following, we separately present the main sea variables.

#### 3.3.1. Ocean Color

The ocean color (OC) is determined by the concentration of the phytoplankton, organic materials, and sediments, as well as anthropogenic materials such as sewages and fertilizers, which provide a nutrient base for organisms in the coastal ocean (e.g., [136,144–147]). It is therefore a key variable to investigate the primary productivity in the upper layers of the coastal zones, together with the phenomena such as the mesoscale eddies (circular currents on the ocean spanning 10 to 100 km in diameter, which persist from a few days up to months), fronts (boundaries between distinct water masses), upwellings (where deep cold water rises to the surface), and internal waves (e.g., [148–152]).

To study the OC, two types of instruments are needed: (i) multispectral radiometers, sensitive to a narrow, discrete wavelength band, ranging between 0.94 and 2.26 μm, and (ii) imaging spectrometers, sampling across the spectrum with a defined spectral resolution.

Small satellites can also be a powerful option to monitor narrow regions at high spatial resolutions, in various spectral ranges [135], e.g., coastal areas to track anthropogenic

and pollutant compounds, on a daily basis and at a ground resolution of a few hundred meters [153,154]. For instance, OC measurements are the main goal of CubeSats, such as SeaHawk-1 (belonging to the SOCON constellation) [155] and ZACUBE-2 [156], with ground resolutions better than about a hundred of meters.

#### 3.3.2. Sea Surface Temperature

The sea surface temperature (SST) is a critical input to study the sea current systems, eddies, jets, and any upwelling in coastal areas, if measured with a sensor accuracy of at least 0.5 K, which is not yet reachable by small satellites (e.g., [157,158]). In addition to being a tool for monitoring sea phenomena and bacteria activities, SST variation in space and time is used for weather forecasting and for maritime services, as well as for studying the sea–atmosphere interactions [158].

SST can be passively measured from the radiometric TIR or MW components of the electromagnetic spectrum. Examples of radiometers operating in the TIR range are MODIS, onboard NASA Aqua and Terra, and AVHRR, onboard the European MetOp and NOAA Polar Orbiting Environmental Satellites (POES), which can provide a global coverage within 1–2 days at a spatial resolution down 1 km [159]. However, TIR acquisitions depend on a clear sky without clouds or volcanic dust. Alternatively, for guaranteeing all-weather continuous acquisitions, SST can be obtained from radiometer data taken at 4 to 12 GHz, because it is proportional to the surface radiance in this frequency range [160]. However, microwave emissions from the sea surface are weak and coarser in resolution (46 km), and the first high-quality data were possible with the Microwave Imager onboard the Tropical Rainfall Measuring Mission (TRMM), a large space mission [160,161].

#### 3.3.3. Sea Surface Salinity

Sea surface salinity (SSS) represents the quantification of salts dissolved in seawater [162]. It is thus a key parameter to measure variations of the fresh water amount within the ocean, as, for instance, a sudden entry of non-salty water through precipitation or melted ice [163] can affect ecosystems. SSS is fundamental for tracking horizontal and vertical water mass movements and/or mixing [163–165]. In particular, SSS, together with SST, can be used to derive ocean density, and, therefore, salinity allows to estimate the long-term variations of the water cycle, ocean–atmosphere exchanges, and the density-driven global ocean circulation [163,165].

The first map of SSS on a global scale, at 40–150 km spatial resolution, was made possible via remote sensing by means of the ESA Soil Moisture and Ocean Salinity (SMOS) mission, launched in 2009, the NASA Aquarius mission, launched in 2011, and the NASA Soil Moisture Active-Passive (SMAP) mission, launched in 2015 [164,166]. SSS is derived from the polarized brightness temperature, which is measured by a radiometer at the L-band, once the dielectric constant of sea water is known [167]. By combining the measurements obtained by sensors onboard all these missions, it is possible to enhance by ~30% the global salinity map [162].

#### 3.3.4. Altimetry: Sea Surface Wind and Height

Altimetry has been used to retrieve surface topography (including sea level and wave height), ocean currents, and bathymetry (submarine topography) (e.g., [168,169]). Additionally, it is one of the most reliable ways to observe mesoscale eddies, detected through the small displacements of the sea surface elevation, and scalar wind speeds (e.g., [170]). The most common instruments for altimetry are nadir pointing radar altimeters, sampling along the ground track (e.g., [168,171]). The radar signal is assembled in a waveform of 20 Hz frequency (~300 m along track), where the peaked waveforms correspond to a low sea state condition, whereas broad waveforms correspond to high sea state conditions.

The sea surface wind (SSW) field is a key parameter affecting oceanic and atmospheric processes. Satellite-derived sea surface wind observations are currently routinely used in a wide variety of oceanic, atmospheric, and climate applications. Within this context, real-

aperture microwave active (i.e., scatterometers [172]) and passive (i.e., radiometers [173]) sensors are widely employed to provide sea surface wind observations to the oceanic and atmospheric operational communities. Although not specifically designed to estimate sea surface wind field, the SAR has been shown to result in reliable enough estimates of sea surface wind field on a finer spatial resolution scale and, therefore, has potential for coastal area applications [174,175].

Sea surface height (SSH) represents the difference of the ocean surface from a constant geopotential surface of reference (level of no motion). SSH is, therefore, key to measuring the thermal expansion and contraction occurring through the different seasons, or to providing information on tides and wind, e.g., [176]. The wave height is estimated from the extent of the leading edge, and typically averaged every 7 km along the tracks (the so-called 1-Hz sampling rate) (e.g., [177,178]). Initially designed for observations on the high seas, such as the sea level change, ocean circulation, and ocean tides [179], the satellite radar has recently shown its relevance for observations of the coastal regions too [180,181].

Large satellites, such as TOPEX/Poseidon and Sentinel-6, can provide altimetric measurements of the global ocean, but they have been also cooperating with the small satellite series Jason (Jason-1, 2, and 3), equipped with a dual frequencies (C and Ku-band) radar altimeter [182,183], for monitoring the global ocean surface topography and thus measuring variations in the height above the sea surface [184].

However, altimeter-derived SSH measurements can come with large errors due to the rapid variation of the coastal topographic surfaces, leading to complex waveforms that are not accurately analyzed by classical re-tracking algorithms [185]. Mesoscale processes instead require altimetric measurements with high spatial and temporal resolutions. At the same time, measuring satellite altitude requires the ability to accurately and independently determine a satellite's orbital trajectory, e.g., its exact longitude, latitude, and altitude. In more recent years, the Global Navigation Satellite System reflectometry (GNSS-R) technique was introduced to measure ocean parameters such as SSW and SSH [186]. In this case, altimetry calculation relies on the position and timing information obtained from several simultaneous measurements of the entire GPS constellation, distributed over an area of thousands of km across-track [187,188].

### *3.4. Application 4: Posidonia Oceanica Monitoring*

*Posidonia oceanica* (L.) Delile, an endemic seagrass of the Mediterranean Sea, forms extensive meadows, which are among the most efficient ecosystems on the planet in terms of the number of services per area [189–194]. These include the stabilization of the sediment and the mitigation of hydrodynamic stress on the coastline, by protecting it from erosive processes (e.g., [195–199]). At the same time, *P. oceanica* meadows are essential for preserving coastal biodiversity and natural resources, and are serviceable for nursery grounds and fish habitats [193,200,201]. Additionally, they represent one of the largest carbon supplies in the Mediterranean Sea [201,202] and other shallow coastal areas across the world [203].

*P. oceanica* meadows can extend from the surface down to 35–40 m deep, depending mostly upon water transparency, and they colonize multiple substrates (e.g., [195,196,204]). The variation of the geomorphological, chemical, and physical characteristics that follow one another along the environmental gradients (e.g., bathymetric variations) determine very heterogeneous grasslands in terms of density, biomass, and associated fauna (e.g., [204]). In recent decades, *P. oceanica* underwent a gradual areal regression, by as much as ~34% in the Mediterranean basin, and 25% in the Italian seas, when comparing historical and the early 2000s maps (e.g., [205]). This regression was caused by anthropogenic processes including fish farm activities, such as trawling and anchoring, gas pipeline refilling, and polluting agents in the coastal areas [198,205–208]. An updated database is thus crucial to study the evolution of the ecosystems formed by the meadows [209], and to safeguard and manage such habitats and biodiversity [189,210].

Remote sensing would be very effective in obtaining a spatial and temporal survey of the meadows, through the generation of a broad and synoptic view of the coastal system, and a complete study of biotic and abiotic variables [200,211–214]. Aquatic ecosystems are indeed characterized by strong optical signals deriving from the distinctive photosynthetic pigments of the various plant groups, from phytoplankton to submerged or emerged macroalgae, from marine phanerogams to coastal-terrestrial plants [215]. However, a good optical depth of water is a necessary condition for mapping the meadows on the sea floor, urging the emergency of contrasting coastal pollution and anthropogenic activities [200]. The evolution of the *P. oceanica* and their erosion can be then modelled from the optical images (once they have been geometrically and radiometrically corrected, e.g., [213]) by means of machine learning techniques (e.g., [216–218]). Additionally, biotic properties of meadows (primary production and density) and abiotic factors (turbidity, bathymetry, and the presence of suspended solids) can be identified in the processed images as geomorphological characterization of the coastal area (e.g., [194]).

The predicted complexity and diversity of the *P. oceanica* environment requires spatial resolutions down a few meters (e.g., [219]). For a detailed *P. oceanica* mapping, remote sensing images at a spatial resolution of about 1 m at nadir in the panchromatic (0.45–0.8 μm), and 2 m at nadir in the multispectral filter band are demanded for an accurate mapping of the meadows. At the same time, a high spectral resolution is required for a finer ocean color acquisition and the correct identification and mapping of the grassland. The multispectral band should include eight filters: (i) 'Blue' (0.45–0.51 μm) and (ii) 'Green' (0.51–0.58 μm), which are reflected by the water column and leaves of *P. oceanica*, with peak reflectivity of the leaves at 0.53 μm; (iii) 'Red' (0.63–0.69 μm), which is strongly absorbed by the water column; (iv) 'Near InfraRed 1' (0.77–0.895 μm), the wavelengths of which have the lowest water absorption, while being strongly reflected by the meadows' leaves; (v) 'Coastal Blue' (0.4–0.45 μm), whose penetrating power into the water and its additional contribution for the atmospheric correction would allow for the identification of coastlines and the analysis of bathymetry; (vi) 'Yellow' (0.585–0.625 μm), which better renders the natural colors of images, and thus allows to optimize the classification processes; (vii) 'Red Edge' (0.705–0.745 μm), which is fundamental for the in-depth analysis of the health of the vegetation covering the wavelength range most affected by the chlorophyll content; and (viii) 'Near InfraRed 2' (0.86–1.04 μm), which is poorly affected by atmospheric conditions, and therefore extremely useful in supporting the analysis of vegetation, as it allows to increase the discriminatory capacity with other habitats.

The latest generation of sensors onboard large (e.g., QuickBird 2 [220,221] and WorldView [221,222]) and medium (e.g., Ikonos [223] and Ikonos-2 [211,220]) satellites have spectral and spatial resolution sufficiently high to obtain a very detailed map of the *P. oceanica* (down to the meter-size resolution, e.g., [201]). However, their time resolution is not sufficient for mapping the spatio-temporal changes of the meadows or to systematically study the coastal and estuarine bio-physical dynamics (e.g., [201]). A short revisiting time (daily to weekly order) does not guarantee the observability of the study area, caused by cloud coverage and/or water turbidity after rainfalls. Therefore, the shorter the revisiting time, the better and more detailed the mapping of *P. Oceanica,* to detect possible dangerous regressions. The constellation of SmallSats can thus be the best solution to satisfy such multi-temporality characteristics, although current small satellites, such as the RapidEye constellation [201,222,224,225], still might not reach the satisfactory spatial resolutions, and new design should be considered for the next SmallSat generation (e.g., deployable optical systems).

### *3.5. Application 5: Precipitations in the Mediterranean Basin*

The Mediterranean basin was defined as a "hot-spot" by [226], being one of the most responsive regions to climate changes. Different global and local scale studies agree on both a rainfall decrease and a growing trend of the minimum and maximum temperatures (e.g., [227–229]). Models also foresee long dry periods, interrupted by extreme intense

summer precipitations, increasing flooding risks (e.g., [230]). Therefore, ameliorating the quality and quantity of the monitoring network represents an asset in order to reduce the effects, and the damages, of extreme weather events.

Precipitation is one of the key measurements, but it is also extremely hard to access the space and time scales of interest and/or because of the complexity or inaccessibility of the studied area (e.g., [231]). Although ground-based weather radars allow to monitor precipitation variability, they are not uniformly and/or sufficiently densely distributed, and gaps for monitoring cloud dynamics on large vertical extension can be filled only by remote sensing observations (e.g., [232]). The Italian Constellation of small satellites for Mediterranean basin Observation (COSMO-SkyMed), First and Second Generations, are medium-large satellites equipped with SAR instrumentations for EO-focused disaster monitoring, including the one caused by flooding [233,234]. Precipitation measurements in the Mediterranean region are currently limited to just a few missions [235], such as the Global Precipitation Measurement mission (GPM) and TRMM, both being large satellites (e.g., [236–239]). In the last few years, the advacement in the miniaturization technology for space instruments has made small satellites an alternative to the larger ones [240]. In particular, CubeSats, such as the NASA Earth Science Technology Office RainCube, TEMPEST-D, and TROPICS, have been developed with specific meteorological goals [51,65,241,242]. Such missions provided useful information on storm structure and distribution, but their high-cost infrastructures are not counterbalanced by a satisfactory scientific return in terms of data temporal resolution for a continuous and real-time characterization of the fast-changing vertical structure of convective cells (e.g., [243–246]). Constellations of small satellites (e.g., NASA CYGNSS) could be a cost-effective solution that can provides meteorologica data with high temporal sampling [247].

Remote sensing payloads suitable to measure the precipitation distribution host a Ka band radar (e.g., [248]). The monitoring of the rainfall in the Mediterranean area can be ensured by a Ka (35.75 GHz) weather radar, with a horizontal resolution of 5 km (or better), a time resolution of 30 min (or better), a vertical resolution of 250 m, and a sensitivity of 20 dBZ. Such requirements are consistent with time and spatial scales of thunderstorm cloud formation (from early to decaying stage) (e.g., [244]). It is necessary to rely on a swath of 500 km and a maximum speed at ground of 5 km/s on a low Earth orbit. Thus, a dense constellation of mini-satellites providing high revisiting times in the entire Mediterranean area could be an effective and less expensive alternative to the current missions.

A typical output of this application consists of reflectivity measurements collected at different altitudes within the tropospheric columns, called the Vertical Profile of Reflectivity (VPR) (e.g., [249]). A quality control chain is needed to remove random and systematic errors, including the correction of the vertical reflectivity profiles (i.e., removal of bright band effects), and the mitigation of attenuation along the path (e.g., [250–252]). This quality control procedure is propaedeutic for a proper validation of the measures, performed through reflectivity data collected by traditional ground-based weather radar, and for a real time application inherent to the monitoring of precipitation events.

### *3.6. Application 6: Earth Observation for Vessel Detection*

Marine vessels detection is currently a very hot topic because it represents a key asset in different domains, e.g., maritime traffic monitoring, surveillance, and smuggling (e.g., [253]). Those vessels that do not voluntarily report any information about their identity, vessel type, route, etc. can be detected and tracked only under a non-cooperative system. Radars or visual surveillance standard methods are usually adopted for vessel non-cooperative detection. A non-cooperative system, which calls for all-day and all-weather capabilities, large area coverage, dense revisiting times, and fine spatial resolution details, is thus a key asset to provide added-value products for the end-users (e.g., policymakers, local authorities, etc.) [254].

Vessels SAR observation is a well-established and mature application, and it is unanimously recognized as one of the most suitable remote sensing tools because it can meet

most of the above-mentioned requirements, in addition to operating in all weather and lighting conditions (e.g., [255–258]). Indeed, most of these systems work in the X-band of SAR payload, with resolutions of the order of the meters, such as for instance the TerraSAR-X satellite, and its twin TANDEM-X [259,260]. Very high resolution (VHR) instruments are able to provide extremely detailed images of the observed scenes (e.g., [261]). The limitations of SAR satellites, such as the long revisiting time, are overcome by using a constellation of micro and nano satellites, which are able to provide VHR images with revisiting times of the order of 2 to 3 h, and at lower costs (e.g., [84,262]), such as Capella X-SAR and ICEYE constellations [57].

In SAR images, the vessel signature appears as a spot brighter than the background due to the vessel scattering, i.e., direct reflection from areas perpendicular to the radar beam, corner reflections, and multiple reflections from the vessel and sea surface [255]. In addition, when imaged by fine spatial-resolution SARs and under specific weather-marine conditions, waves associated with moving vessels can be also observed in the data.

However, radar images suffer from large intrinsic noise (speckle), in addition to the azimuth displacements ("train-off-the-track effect"), which are caused by the Doppler effect, and the azimuth ambiguity patterns ("ghost"), which are weaker, repetitive artefacts appearing in coastal areas, caused by the presence of brighter objects on the mainland (e.g., [263]). False positive detections can occur in non-homogeneous areas of the images due to changes in ocean backscattering or to oceanographic phenomena, e.g., atmospheric fronts, internal waves, current boundaries, breaking waves, outlying rocks, shoal sea currents, and coastal effects, while high wind and rough sea states can hamper the correct identification of small vessels [255,264].

The comparison of the pre- and post-event images collected by the micro-satellites can provide an efficient method to detect map changes, robust both to speckle phenomena and co-registration problems (e.g., [265]). In order to increase the accuracy of vessel detection, X-band SAR data are processed through four fundamental stages: land masking, pre-processing, pre-screening, and discrimination [255,266]. Such processing allows the presence of a non-negligible coherent component in the backscattered sea surface signal to be highlighted by evaluating the corresponding Rice Factor (RF) image of the area under study [267]. The RF represents the coherent-to-incoherent received power ratio of the backscattered signal, and therefore the pre-processing stage consists in evaluating the RF of the calibrated SAR image. The pre-screening stage is based on a vessel search by applying the "bright anomalies" method on the RF images [255,268]. Because it was proven that the RF image follows a log-normal distribution, a threshold can be straightforwardly set according to a constant false alarm rate (CFAR) approach to remove false positives [266].

A similar approach is also used for change detection (CD) in urban areas, which adopts a convolutional neural network (CNN) algorithm to process the SAR-generated dataset and retrieve changes of urban structures and buildings (e.g., [269]).

### *3.7. Application 7: Sea State from SAR and Instrumentation Located Onboard the Vessel*

As shown in the previous chapter Section 3.6, remote sensing observations represent a powerful tool for providing the kinematic properties of vessels. In turn, the ship motion analysis allows for the real-time assessment of the sea state parameters, which can contribute to minimizing the navigation risks by supporting the onboard decision to handle potentially dangerous phenomena in following and quartering seas, such as surf-riding, broaching, and parametric rolling, and to reduce the fuel costs (e.g., [270,271]). Sea state condition monitoring improves the statistics of long-term wave data, providing additional information, especially in open ocean waters, where the weather buoys are very scattered [272]. In addition, it allows to optimize the ship route by balancing variations of the weather conditions and navigational constraints [273]. Additional benefits arise from the assessment of the onboard comfort level, mainly related to the motion sickness incidence (MSI) parameter, which needs to be continuously monitored to increase the seakeeping performances of passenger ships [270,274].

The characteristic parameters of the sea waves can be efficiently determined from SAR imaging systems, because they are operative in all the light and weather conditions and have a wide swath. The radar system needs an X- or C-band, with a resolution better than a few tens of meters. So far, several large (e.g., the pioneer USA SeaSat [275], ESA Sentinel-1 [276], and DLR TerraSAR-X [259]) and medium-large (e.g., Italian COSMO-SkyMed [233,234]) satellites have been employed to accurately estimate the wave parameters, such as height, average length, and direction, using SAR system in various bands, e.g., C-, X-, and L-bands [277,278]. However, despite their lower swath and space resolution, small platforms are taking hold (e.g., UK NovaSAR-1 and Israeli TecSAR [57]), thanks to the opportunity of multiple launches and the use of non-sun-synchronous orbits [57].

The characteristic parameters of the sea waves provided by the SAR system mounted on small platforms can be used as references to verify the performance of a parametric wave spectrum resembling procedure that can be applied to detect the sea state parameters based on the measurement and analysis of the heave and pitch motions of a vessel in a seaway, recorded by positioning sensors located onboard the ship [279,280]. In detail, the heave and pitch motions in a seaway can be estimated starting from the survey of the amplitudes of the ship vertical motions in a point of known coordinates, located on the centerline plane, using the GNSS (Global Navigation Satellite System), and pitch acceleration, using a gyroscope [281,282]. The pitch acceleration allows to determine the pitch motion amplitude of the ship (by double integration in the time domain), and, from the vertical translational motion (composed by heave and pitch motions), it is possible to compute the heave motion amplitude of the center of mass. These data allow to determine the response spectra related to the heave and pitch motions in the encounter wave frequency domain [280,281,283]. The response spectra as a function of the absolute frequency can be evaluated on the basis of two additional input data, namely the vessel speed, which is measured by the GNSS, and the encounter angle between the true course of the ship (determined by GNSS system) and the prevailing direction of the sea, which is derived from images obtained by the SAR systems. Given both the response spectra and the ship complex transfer functions, it is possible to determine the sea spectrum by generating the motions [282]. Finally, from the spectral distribution of the sea in the absolute frequency domain, the characteristic parameters are obtained, namely, significant wave height, wave peak period, and spectrum peak enhancement factor.

The idea is to use the radar imaging systems mounted on the micro-satellites constellation, which are to be integrated with the GNSS and the instrumentation on board, in order to provide an integrated ship monitoring system, which can be considered as a mobile laboratory capable of carrying out in situ measurements for the estimation of ship motions and, subsequently, to derive the characteristics of the incident wave (e.g., [270,279,281,282]).

## 4. Data Fusion Techniques Applied to Remote Sensing Data

The heterogeneity of the study cases presented in the previous chapter highlighted the advantage of using remote sensing for investigating various environments and aspects of the Earth surface by means of a number of different sensors, each one gathering different intervals of the electromagnetic solar flux reflected back by the surface, and varying in terms of spatial and spectral resolutions [284,285]. Optical sensors in the VIS to NIR spectral range may better serve for mapping horizontal patterns, and SAR systems allow to characterize the targets in all weather conditions, whereas LiDAR technology provides for accurate vertical profile measurements (e.g., [284]). At the same time, the revisiting capability of the satellites allowed to include the temporal information to a given 2D scene [286]. This additional information provided by space-born sensors enables to monitor the evolution of a certain process or of a natural disaster, and/or the variation over time of a certain area [287]. One explicative example is given by the case of *P. Oceanica* (chapter §3.4), whose mapping at various times allows to appraise the eventual active degradation processes, and to establish mitigation plans.

The growth in the number and variety of both space platforms and remote sensing sensors has opened the path to new techniques of data analysis, which can provide more reliable, coherent, and comprehensive information about the observed scene [286,288]. The data fusion approach thus relies on coupling observations acquired by different sources, whose joint analysis can favor a better interpretation of a certain process or of the observed scene, because the resulting fused data encompass more detailed information than each single acquisition, merging together all the meaningful information acquired by the different sensors (e.g., [284,289–292]). Data fusion techniques enable for the monitoring of fast-evolving environmental processes, e.g., highly dynamic natural processes such as polynyas [132], climate changes [293], desertification processes [294], deforestation [295], coastal erosion [296], and the phases of urban development [297], as well as object recognition and tracking or classification, and change detection [288].

Data fusion has been firstly adopted to blend the high spatial resolution of PAN with the high spectral resolution of MS acquisitions [287]. The accessibility to both the panchromatic and usually four multispectral bands will enable the application of pan-sharpening techniques, and the consequent availability of multispectral data at the same geometric resolution as the panchromatic. Indeed, due to their constructional constraints, MS sensors have a very narrow spectral bandwidth, which in turn requires a larger instantaneous field of view (IFOV), and are thus characterized by a lower spatial resolution than PAN sensors [284,285]. On the contrary, the smaller IFOV of PAN sensors allows to achieve better spatial resolutions, but their broader bandwidths do not allow to reach high spectral resolutions. Such a distinctiveness in the bandwidth properties of PAN and MS images means that a single sensor is unable to simultaneously have both high spatial and spectral resolution [284,292]. Nevertheless, both PAN and MS sensors simultaneously acquire the same ground scene, with the same acquisition mode too, facilitating the synthesis of the PAN high spatial resolution with the MS high spectral resolution properties [284]. This is the so-called pan-sharpening technique, which stands for its key role for producing high-resolution multispectral images (e.g., [284,292,298–300]), opening to the possibility of mapping the territory at the highest resolution and of having color ortho-images comparable to those obtainable from aircrafts, which becomes particularly useful for land cover classification, visual interpretation, and target recognition [284,286].

The strength of the data fusion approach can be appraised when considering different types of instruments. For instance, the fusion of multispectral satellite imagery and LiDAR data allows for an accurate object recognition and classification, when the spectral signature is supported by the altimetric variations provided by the digital elevation model [287,301]. Another useful multi-instrument data combination relies on fusing optical images with SAR data, which, being based on radar backscatter measurements, extend the information on the observed scene acquired in the VIS to NIR spectral bands, especially when the cloud coverage causes gaps in the time series of any continuous monitoring [284,286,287].

On the other hand, another convenient data fusion technique is related to the revisit capability characterizing spaceborne instruments, which can acquire the same ground area with a frequency of up to a daily basis (e.g., small satellites in constellation configuration, cf. Table 2) [286,302]. The spatio-temporal fusion allows to *fuse* low spatial/high temporal resolution data with high spatial/low temporal resolution data, providing multitemporal high spatial-resolution data. This data fusion, which benefits from the data acquired in the same acquisition mode reducing any co-registration issues, allows for applying change detection techniques to monitor highly dynamic processes, including hazard handling [284,286,287,292]. Similarly, the spectral and/or back-scattering data can also be integrated with the temporal data [286].

The fusion of data acquired at different times from the same sensor or different sensors, such as VIS–NIR optical, SAR, and LiDAR instruments, enables the creation of a comprehensive 4D representation of the observed ground scene [284,286,302]. The initial set of data used for fusion and/or the degree of information to be extracted from the final

output determine the data fusion level: (i) raw data level (e.g., pan-sharpening), where the input data from the various sources are integrated into one single, higher spatial resolution data; (ii) feature level (e.g., classification and change detection), where surface features can be extracted and re-arranged; and (iii) decision level (e.g., fusion of data acquired by multiple sensors—optical, SAR, and LiDAR), where the results from multiple algorithms are combined and fused into one single, fused decision [284,287,288]. Such an increase in the degree of data fusion level brings the current trend out, where this approach has become a fundamental tool for data analysis, partly due to the increase in the number of the launched satellites (eventually in constellation configuration), to the improvement of the spatial and spectral resolutions of space sensors, and to the opportunity of validating and integrating the remote sensing data with ground data [284].

In this framework, the DORA project can greatly benefit from the data fusion techniques outlined above. On one hand, the current telescope prototype under development is equipped with an optical sensor operating in the VIS to TIR spectral bands, for which the various study cases requested a ~300–400 nm panchromatic filter and several ~50 nm multispectral filters. On the other hand, a similar instrument equipped instead with an SAR antenna is under study, as well as the possibility of having a constellation of small platforms flying deployable optics. At the present state of activities, with only the optical sensor under development, we will consider here only the pan-sharpening technique for the data fusion application.

So far, large satellites, such as the WorldView, have optical sensors with very high resolutions (of the order of a meter or less) and multiple spectral bands, which allow for the pan-sharpening technique. However, since its initial conceptualization, data fusion has become an essential tool to process data acquired by small satellites, which can (i) guarantee a great ground coverage by means of constellations, and (ii) ensure a wider utilization of the final data products, because they are cheaper. An example can be provided by the SkySat constellation (in the case of SkySat 16 to 21, the resolutions of the panchromatic and the spectral bands are 0.57 m and 0.75 m, respectively). See Table 2 for more examples.

Here, we present the results of pan-sharpening applied to panchromatic and multispectral images taken by Pléiades HR-1B, a large satellite that acquired images at the spatial resolutions of 0.5 m and 2 m for the panchromatic and multispectral filters, respectively, i.e., similar to those achievable with small satellites. Figure 1, showing the RGB composition of Lesbos Island (Greece), is taken as a sample image, where four pan-sharpening techniques are tested: multiplicative, simple mean, intensity hue saturation (IHS), and Brovey transformation. Figure 2a–d show the same scene of Figure 1 in RGB, each one after the application of one of the pan-sharpening techniques listed above. Because the best performing method cannot be fixed in an absolute way, but depends on the characteristics of the study area, several methods must be compared each time to select the one which provides suitable results for a defined purpose, by means of visual, spatial, and spectral analysis [303,304].

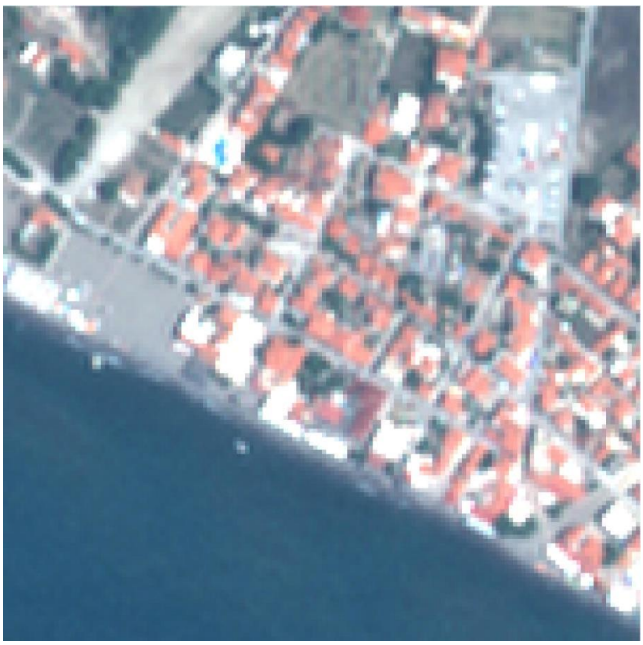

**Figure 1.** RGB true color composition of a semi-urban area in Lesbos Island (Greece). Taken by Pléiades HR-1B instrumentations, which has a resolution of 0.5 m in the panchromatic and 2 m in the multispectral filters. The picture shows that the area taken by the instrument is at low resolutions, and details cannot be appreciated.


**Figure 2.** The image of the same region in Figure 1, after being processed by pan-sharpening techniques: (**a**) multiplicative method, (**b**) simple mean method, (**c**) IHS, and (**d**) Brovey transformation.

## 5. Radiometric Model as Tool for DORA Feasibility Study

In this paper, we have presented a selection of study cases that are not exhaustive of all the possible marine, atmospheric, and oceanographic research topics, but they have been selected for being quite wide-ranging to carry out the feasibility study of the DORA project. In Table 3, we summarize the state-of-the-art of the presented study cases, which will highlight how new space missions, such as the one studied within the DORA project, can be of great benefit for their investigation and progress. Indeed, current remote sensing data are only partially available because of the high costs of the large satellite data acquisition and/or the still limited use of small satellites.

**Table 3.** Summary of the study cases presented in Section 3. The forth column reports the current available data to study the specific research case, whereas the last one shows what it is still missing for a complete understanding of the related topics.

| ID | Scientific Area | Goals | State-of-the-Art | What We Need |
|---|---|---|---|---|
| *A1* | *Composition of the atmosphere ($SO_2$)* | Continuous monitoring of traces gases, e.g., $SO_2$, from natural (volcanic) and anthropogenic (traffic, industry) sources | Large satellites (e.g., ESA Sentinel, NOAA/NASA POESS, or EUMESAT MetOp programs) and recently small satellites (e.g., PARASOL, HARP, and MIOSat) were inserted into polar and geostationary orbits to monitor the atmosphere | • Having the payload on a constellation of small satellites allows for a short revisiting time, critical to study real-time evolution of natural and anthropogenic events<br>• MEMS technology can be used on integrated chips, avoiding complex and heavy mobile optics |
| *A2* | *Polynyas monitoring in polar areas* | High resolution continuous monitoring of polynyas dynamics to study the evolution of the seasonal ice production | MODIS onboard Aqua EOS has a short revisiting time, but a low spatial resolution (1 km) | A short revisiting time provided by a constellation is associated with higher resolution to investigate the small-scale variability that characterizes the ice-water border |
| *A3* | *Coastal area monitoring* | Ocean color, sea surface temperature monitoring, and the sea state and altimetry | Available data are not at resolutions of space and time needed to have a comprehensive monitoring of the dynamics and variability of coastal natural phenomena | Monitor narrower regions, allowing the acquisition of data at higher spatial resolution (few hundred meters), in various spectral ranges, on a daily basis, allowing for instance to track the evolution of pollutant spillage |
| *A4* | *P. oceanica monitoring* | Before a gradual regression over the whole Mediterranean basin, an update of the dynamics and extension/distribution variation is needed | Instruments onboard large or medium sized satellites (e.g., QuickBird, WorldView, and Ikonos-2) have high spectral and spatial resolution for mapping the meadows, but long revisiting times | • Remote sensing images at spatial resolution of 1 m (PAN) and 2 m (MS), with a revisiting time of 5 days (on the nadir) and 7–8 days (off-nadir): (i) systematic monitoring of meadows, (ii) study of the coastal and estuarine biophysical dynamics<br>• Marine Protected Areas effectiveness |
| *A5* | *Precipitations in the Mediterranean basin* | The Mediterranean basin is a hot-spot: measuring vertical precipitation profiles in this area can be of essential relevance for capturing the entire development process of a thunderstorm clouds and, therefore, to reduce their impacts | In many regions, such as the Mediterranean basin, precipitation surveillance networks are still incomplete and inadequate: available data consist of rain-gauges punctual measurements, or ground-based weather radar, and very few satellite missions (e.g., TRMM) | Data with spatial and temporal resolutions good enough for a continuous and real-time characterization of fast-changing vertical structure of convective cells originated during extreme rainfall in the Mediterranean region |

**Table 3.** *Cont.*

| ID | Scientific Area | Goals | State-of-the-Art | What We Need |
|---|---|---|---|---|
| *A6* | *Sea state from the vessel motions analysis* | • Continuous monitoring of sea state conditions to improve the statistics of long-term wave data and optimize the route by balancing variations of the weather conditions and navigational constraints<br>• Develop an integrated ship monitoring system, based on the integration of satellite positioning and radar imaging methods for determining the sea spectrum starting from the survey and analysis of vessel motions | SAR imaging (e.g., Sentinel-1, TerraSAR-X) to accurately estimate the wave parameters such as height, average length, and direction | • Radar imaging<br>• GNSS and onboard instrumentation to determine the sea states from the ship movements<br>• Daily/hourly revisiting time |
| *A7* | *EO for vessel detection* | All-day and all-weather capabilities, large area coverage, dense revisit time, fine spatial resolution details are key assets to generate added-value products to be delivered to end-users (e.g., policymakers, local authorities) | SAR observation of vessels is a well-established and mature application | The possibility of having a constellation of platforms with a very short revisiting time (2–3 h) VHR images at lower costs |

Generally, for all the cases considered here, the remote sensing system should include instrumentation operating in the spectral range from VIS to NIR and in MW range, and on a global coverage, in order to accurately investigate and monitor the terrestrial environment. Such a system might be launched on a small satellite (mass $\leq$ 100 kg), operating on a circular polar orbit, with an altitude of ~400 to ~800 km (LEO), resulting in an orbital speed of ~7.5 km/s, which corresponds to a 6.91 km/s ground speed. The orbit should be also heliosynchronous, with an orbital period of about 100 min, i.e., about 15 orbits in one day, and equatorial passes at ~10:00 ÷ 14:00 local time.

We performed a feasibility study only of those applications that demanded a sensor in the VIS to IR spectral range. We carried out a radiometric analysis on the system, which allowed to quantify the radiation flux gathered by the optical system, at varying observing conditions and needed resolutions, and the signal-to-noise ratio (SNR). The SNR is then compared to the specific values given by each application to determine whether or not DORA can reach the requested requirements. In Table 4, the columns 2 to 5 and 7 summarize the requirements, from each of the applications listed in Section 3, to accomplish their specific goals. We also included for completeness the MW-related applications, listing all their requirements, and for a couple of them we assessed their feasibility.

To evaluate the characteristics and performances of the optical instrument, a radiometric model has been developed. The core of such a model represents the response of the instrument, by correctly assessing the spectral response of all its constituting optical elements [305]. On the other hand, the final signal gathered by the detector also depends on the observed sources, which varied from one application to another, and the targets of which have been thus used to compute the output signal and related SNR. Due to the lack of a physical model of the instrument we are considering, in order to produce reliable and meaningful results, the spectral properties of the instrument were assumed based on previous similar projects or instruments in operation [305,306].

**Table 4.** Measurement requirements of the case studies presented in Section 3.

| 0 | 1 | 2 | 3 | 4 | 5 | 6 | 7 | 8 | 9 |
|---|---|---|---|---|---|---|---|---|---|
| **ID** | **Scientific Area** | **Albedo** | **Measure Kind** | **Spectral Range (μm When Not Explicitly Written)** | **Minimum Ground Resolution (m/pix)** | **Maximum Integration Time (ms)** | **Requested SNR** | **Model SNR [a]** | **Optimal Ground Resolution (m/pix) [b]** |
| *A1* | *Composition of the atmosphere: $SO_2$ and $NO_2$* | 0.43 | spectral measures in UV–VIS–IR | 0.308 ($SO_2$) | 100 | 10.13 | 50–100 | 47 | 200 |
| | | | | 0.434 ($NO_2$) | | | | >few hundreds | 20 |
| *A2* | *Polynyas monitoring in polar areas* | 0.75 | 2 spectral bands in SWIR | 1.075–1.125 | <10–150 * | 50.65 | 100 | >few hundreds | 5 |
| | | | | 1.175–1.225 | | | | | 50 |
| *A3* | *Coastal area monitoring: ocean color* | 0.10 | 12 spectral bands in VIS–NIR (0.4–1.0 μm) | 0.400–0.450 | 30–100 * | 3.04 | >few hundreds | >few hundreds | 30 ** |
| | | | | 0.450–0.500<br>0.500–0.550<br>0.550–0.600<br>0.600–0.650 | | | | | 25 |
| | | | | 0.650–0.700<br>0.700–0.750<br>0.750–0.800<br>0.800–0.850<br>0.850–0.900<br>0.900–0.950<br>0.950–1.000 | | | | | 15 |
| | | 0.10 | 12 spectral bands in SWIR (0.9–2.5 μm) | 1.000–1.125 | 30–100 ** | 3.04 | >100–200 | >few hundreds | 10 |
| | | | | 1.125–1.250<br>1.250–1.375<br>1.375–1.500<br>1.500–1.625<br>1.625–1.750<br>1.750–1.875<br>1.875–2.000 | | | | ~35 ÷ 60 | 60 |
| | | | | 2.000–2.125<br>2.125–2.250<br>2.250–2.375<br>2.375–2.500 | | | | ~30 ÷ 35 | 80 |
| | *Coastal area monitoring: ocean altimetry* | - | radiometer | Ku-band<br>C-band | 50–100 ** | - | <20 | - | - |
| *A4* | *P. oceanica monitoring* | 0.1 | 1 panchromatic filter | 0.450–0.800 | 1 | 0.10 | 100 | 22 | 3 |
| | | | 8 spectral bands | 0.400–0.450<br>0.450–0.510<br>0.510–0.580<br>0.585–0.625<br>0.630–0.690<br>0.705–0.745<br>0.770–0.895<br>0.860–1.040 | 2 | 0.20 | 100 | ~20 ÷ 40 | 6 |
| *A5* | *Precipitations in the Mediterranean basin* | - | Punctual | Ka-band (35.75 GHz) | Hor. Res.: <5000<br>Vert. Res.: <250 | - | 20 dBZ | - | |
| *A6* [c] | *Sea state from the vessel motions analysis* | - | Single-pol either VV or HH | X- or C-band | <10 | ≈0.5 s (standard for SAR | Better than −20 dB | - | 5 |
| *A7* | *EO for vessel detection* | - | Single-pol (HH)/dual-pol (HH + HV)− | X- or C-band | <10 | ≈0.5 s (standard for SAR | −20 dB | - | <5 |

[a] The "model" SNR was derived considering the minimum ground resolution requested by the specific application. [b] An exploratory study has been carried out to evaluate the optimal ground resolution to satisfy the condition of having a "Model" SNR higher than the requested value. [c] Most of the operational satellite SARs are designed with a specific "wave mode (WM)" that, for instance, in the case of the Copernicus Sentinel-1 mission, collects 20 km by 20 km images at 5 m by 5 m spatial resolution every 100 km along the orbit. * A wider range is considered necessary to be further tested. ** Spatial resolution effectively requested by the specific application.

The radiometric model is developed from the solar radiation flux at the terrestrial upper atmosphere, which was shaped as the Plank function, assuming the sun as a black body at a temperature of 5800 K (BB model), and decreased in intensity to consider the radiation travel to the Earth's orbit. The characteristics of the telescope and platform were assumed on the basis of the most recent optical design. The deployable telescope is assumed with an aperture of 300 m, with an obstruction of 60 mm due to the presence of a secondary mirror. This is coupled with panchromatic and multispectral filters, ranging from about 0.3 to 2.5 µm, with a bandwidth from about 0.05 to 0.2 µm, depending on the considered application. In order to derive the final flux, we considered the optical efficiency (varying between 0.65 and 0.85 in the 350 to 1100 nm wavelength range, and 0.001 otherwise) and the detector quantum efficiency (set to 0.6). The reflected solar flux was obtained by assuming the albedo (which was different for each application, cf. Table 4), whereas no corrective factor was included to account for the terrestrial atmosphere effects, assuming to avoid the stronger absorption bands. The total radiation was derived using the maximum integration time, set to 70% of the dwell time. The SNR was estimated assuming as the main error source the shot noise, and was therefore computed as a square root of the signal.

In Table 4, column 8, the results of the radiometric analysis are provided. We draw attention to the fact that these SNR values are functions of the *maximum integration time*, which is in turn computed from the ground resolutions (depending on the requirements requested by each applications), and the ground track speed (depending on the spacecraft speed and the altitude). We found that the DORA system is capable of resolving the majority of the targets and features described by the various applications. One of the most problematic observations is given by the *P. oceanica*. We therefore performed a parametric study to evaluate the downgrading of the ground resolution (Table 4, column 9) to have an SNR sufficient for observations. In this case, we obtained that *P. oceanica* colonies can be observed and monitored by the DORA system with a ground resolution three times larger than requested.

## 6. Conclusions

In this paper, we reviewed several environmental applications in marine, atmospheric, and oceanographic thematics, and selected both for having pivotal advancements by using remote sensing data and for being quite comprehensive to evaluate the capabilities of deployable optical systems. In particular, we focused on the Deployable Optics for Remote sensing Applications (DORA) project, which is currently under development, and tested its optical performances through radiometric analysis.

The analyzed study cases show how past and current small satellites can be of great benefit to improve such topics, in terms of data resolutions, revisiting times, and lower acquisition costs. On the other hand, manufacturing constraints imposed by small satellites, i.e., size and weight limitations, might severely limit data quality (high spatial and spectral resolutions) with respect to the requirements needed for a specific application. We showed that the DORA deployable telescope is a valuable solution for EO, in particular for monitoring ecological issues, so as to be able to implement arrangements in a timely manner to protect our natural environment.

The successful development of deployable remote-sensing payloads onboard small satellites might also represent a pathway for the exploration of planets and small bodies, whose variety of properties, in terms of size, shape, composition, and internal structure, calls for newer space missions to fill the gaps in the understanding of our solar system.

**Supplementary Materials:** The following supporting information can be downloaded at: https://www.mdpi.com/article/10.3390/rs14092066/s1, Table S1: Lists of all the medium to large space missions cited in the text, reporting all their 34 relevant characteristics for the study cases in the spectral range from VIS to MW. References [43,56,57,63,307–317] are cited in supplementary materials.

**Author Contributions:** Conceptualization, E.M., G.F. (Giampaolo Ferraioli), A.R. (Alessandra Rotundi), V.D.C., P.P., I.B. and L.I.; Data curation, E.M., E.A., L.A., G.A., V.C., E.C. (Elena Catucci), P.D.P., F.E., E.F., A.I. (Anna Innac), S.P., S.S. and G.T.; Formal analysis, E.M., A.M.P., V.D.C., E.A., L.A., G.A., V.C., E.C. (Elena Catucci), P.D.P., F.E., E.F., A.I. (Anna Innac), S.P., S.S. and G.T.; Funding acquisition, V.D.C.; Investigation, E.M. and A.M.P.; Methodology, E.M., A.M.P., G.F. (Giampaolo Ferraioli), V.D.C. and P.P.; Project administration, G.F. (Giampaolo Ferraioli), A.R. (Alessandra Rotundi), P.P., S.C., E.C. (Elena Chianese), P.P.F., G.F. (Giannetta Fusco), S.G., A.I. (Agostino Iadicicco), F.N., C.P., V.P., A.R. (Angelo Riccio), G.F.R. and E.Z.; Resources, E.M., I.B. and Z.D.; Supervision, A.R. (Alessandra Rotundi), V.D.C., P.P., S.C., P.P.F., G.F. (Giannetta Fusco), S.G., A.I. (Agostino Iadicicco), F.N., C.P., V.P., A.R. (Angelo Riccio), G.F.R. and E.Z.; Validation, P.P., I.B. and E.C. (Elena Chianese); Writing—original draft, E.M., A.M.P., G.F. (Giampaolo Ferraioli), A.R. (Alessandra Rotundi), V.D.C., P.P., E.A., L.A., G.A., I.B., V.C., E.C. (Elena Catucci), P.D.P., F.E., E.F., A.I. (Anna Innac), S.P., S.S. and G.T.; Writing—review & editing, E.M., A.M.P., G.F. (Giampaolo Ferraioli), A.R. (Alessandra Rotundi), V.D.C., P.P. and I.B. All authors have read and agreed to the published version of the manuscript.

**Funding:** The work was developed within the framework of "DORA — Deployable Optics for Remote sensing Applications" (project no. ARS01_00653), specialisation area "aerospace", a project funded by MIUR–PON "Research & Innovation"/PNR 2015–2020. The authors received funding from the Department of Sciences and Technologies, University of Napoli "Parthenope" for the OA publication.

**Acknowledgments:** The authors thank the Editor and anonymous Reviewers for critical discussion on this and on an earlier version of the study.

**Conflicts of Interest:** The authors declare no conflict of interest.

## References

1. Canuti, P.; Casagli, N.; Ermini, L.; Fanti, R.; Farina, P. Landslide activity as a geoindicator in Italy: Significance and new perspectives from remote sensing. *Environ. Geol.* **2004**, *45*, 907–919. [CrossRef]
2. De Groeve, T. Flood monitoring and mapping using passive microwave remote sensing in Namibia. *Geomat. Nat. Hazards Risk* **2010**, *1*, 19–35. [CrossRef]
3. Dennison, P.E. Fire detection in imaging spectrometer data using atmospheric carbon dioxide absorption. *Int. J. Remote Sens.* **2006**, *27*, 3049–3055. [CrossRef]
4. Fea, M.; Capaldo, M.; Pesaresi, C. Remote sensing and interdisciplinary approach for forecasting and analysing the effects of hurricanes, tropical cyclones and typhoons. *J. Res. Didact. Geogr.* **2015**, *1*, 117–150. [CrossRef]
5. Geiß, C.; Taubenböck, H. Remote sensing contributing to assess earthquake risk: From a literature review towards a roadmap. *Nat. Hazards* **2013**, *68*, 7–48. [CrossRef]
6. Goldberg, M.D.; Li, S.; Goodman, S.; Lindsey, D.; Sjoberg, B.; Sun, D. Contributions of Operational Satellites in Monitoring the Catastrophic Floodwaters Due to Hurricane Harvey. *Remote Sens.* **2018**, *10*, 1256. [CrossRef]
7. Gonzalez, L.; Briottet, X. North Africa and Saudi Arabia Day/Night Sandstorm Survey (NASCube). *Remote Sens.* **2017**, *9*, 896. [CrossRef]
8. Joyce, K.E.; Belliss, S.E.; Samsonov, S.V.; McNeill, S.J.; Glassey, P.J. A review of the status of satellite remote sensing and image processing techniques for mapping natural hazards and disasters. *Prog. Phys. Geog.* **2009**, *33*, 183–207. [CrossRef]
9. Kaufman, Y.J.; Tucker, C.J.; Fung, I. Remote sensing of biomass burning in the tropics. *J. Geophys. Res.* **1990**, *95*, 9927–9939. [CrossRef]
10. Kunte, P.D.; Aswini, M.A. Detection and monitoring of super sandstorm and its impacts on Arabian Sea—Remote sensing approach. *Atmos. Res.* **2015**, *160*, 109–125. [CrossRef]
11. Mantovani, F.; Soeters, R.; Van Western, C.J. Remote sensing techniques for landslide studies and hazard zonation in Europe. *Geomorphology* **1996**, *15*, 213–225. [CrossRef]
12. Psomiadis, E.; Soulis, K.X.; Zoka, M.; Dercas, N. Synergistic Approach of Remote Sensing and GIS Techniques for Flash-Flood Monitoring and Damage Assessment in Thessaly Plain Area, Greece. *Water* **2019**, *11*, 448. [CrossRef]
13. Sepuru, T.K.; Dube, T. An appraisal on the progress of remote sensing applications in soil erosion mapping and monitoring. *Remote Sens. Appl. Soc. Environ.* **2018**, *9*, 1–9. [CrossRef]
14. Wright, R.; Garbeil, H.; Harris, A.J.L. Using infrared satellite data to drive a thermorheological/stochastic lava flow emplacement model: A method for near-real-time volcanic hazard assessment. *Geophys. Res. Lett.* **2008**, *35*, L19307. [CrossRef]
15. Santilli, G.; Venditozzi, C.; Cappelletti, C.; Battistini, S.; Gessimi, P. CubeSat constellations for disaster management in remote areas. *Acta Astronaut.* **2018**, *145*, 11–17. [CrossRef]
16. Boccardo, P.; Tonolo, F.G. Remote Sensing Role in Emergency Mapping for Disaster Response. In *Engineering Geology for Society and Territory*; Lollino, G., Manconi, A., Guzzetti, F., Culshaw, M., Bobrowsky, P., Luino, F., Eds.; Springer: Cham, Switzerland, 2015; Volume 5. [CrossRef]

17. Corbane, C.; Lang, S.; Pipkins, K.; Alleaume, S.; Deshayes, M.; García Millán, V.E.; Strasser, T.; Vanden Borre, J.; Toon, S.; Michael, F. Remote sensing for mapping natural habitats and their conservation status—New opportunities and challenges. *Int. Appl. Earth Obs.* **2015**, *37*, 7–16. [CrossRef]
18. Hoque, M.A.-A.; Phinn, S.; Roselfama, C. A systematic review of tropical cyclone disaster management research using remote sensing and spatial analysis. *Ocean Coast. Manag.* **2017**, *146*, 109–120. [CrossRef]
19. Kaku, K. Satellite remote sensing for disaster management support: A holistic and staged approach based on case studies in Sentinel Asia. *Int. J. Disaster Risk Reduct.* **2019**, *33*, 417–432. [CrossRef]
20. Klemas, V. The Role of Remote Sensing in Predicting and Determining Coastal Storm Impacts. *J. Coast. Res.* **2009**, *2009*, 1264–1275. [CrossRef]
21. Finckenor, M.M.; de Groh, K.K. A Researcher's Guide to: International Space Station—Space Environmental Effects. NASA ISS Program Science Office; 2019. Available online: https://www.nasa.gov/sites/default/files/files/NP-2015-03-015-JSC_Space_Environment-ISS-Mini-Book-2015-508.pdf (accessed on 22 October 2021).
22. Sweeting, M.N. Modern Small Satellites—Changing the Economics of Space. *Proc. IEEE* **2018**, *106*, 343–361. [CrossRef]
23. Belward, A.S.; Skøien, J.O. Who launched what, when and why; trends in global land-coverobservation capacity from civilian Earth Observation satellites. *ISPRS J. Photogramm. Remote Sens.* **2015**, *103*, 115–128. [CrossRef]
24. Gooding, D.; Richardson, G.; Haslehurst, A.; Smith, D.; Saunders, C.; Aglietti, G.; Blows, R.; Shore, J.; Hampson, K.; Booth, M. A novel deployable telescope to facilitate a low-cost <1 m GSD video rapid-revisit small satellite constellation. In Proceedings of the International Conference on Space Optics, Chania, Greece, 9–12 October 2018; Volume 11180, p. 1118009. [CrossRef]
25. Ehlers, M. Multisensor image fusion techniques in remote sensing. *ISPRS J. Photogramm. Remote Sens.* **1991**, *46*, 19–30. [CrossRef]
26. Kramer, H.J.; Cracknell, A.P. An overview of small satellites in remote sensing. *Int. J. Remote Sens.* **2008**, *29*, 4285–4337. [CrossRef]
27. Botelho A. S., R.C.; Xavier, A.L., Jr. A Unified Satellite Taxonomy Proposal Based on Mass and Size. *Adv. Aerospace Sci. Technol.* **2019**, *4*, 57–73. [CrossRef]
28. Helvajian, H.; Janson, S. *Small Satellites: Past, Present, and Future*; The Aerospace Press: Washington, DC, USA, 2009. [CrossRef]
29. Madry, S.; Pelton, J.N. Historical Perspectives on the Evolution of Small Satellites. In *Handbook of Small Satellites*; Pelton, J.N., Madry, S., Eds.; Springer: Cham, Switzerland, 2020. [CrossRef]
30. Millan, R.M.; von Steiger, R.; Sergey Bartalev, M.A.; Borgeaud, M.; Campagnola, S.; Castillo-Rogez, J.C.; Fléron, R.; Gass, V.; Gregorio, A.; Klumpar, D.M.; et al. Small satellites for space science: A COSPAR scientific roadmap. *Adv. Space Res.* **2019**, *64*, 1466–1517. [CrossRef]
31. Xue, Y.; Li, Y.; Guang, J.; Zhang, X.; Guo, J. Small satellite remote sensing and applications—History, current and future. *Int. J. Remote Sens.* **2008**, *29*, 4339–4372. [CrossRef]
32. Baker, K.; Jansson, D. A Brief History of AMSAT. Available online: https://www.amsat.org/amsat-history/ (accessed on 22 October 2021).
33. Bonometti, R.J.; Nicastri, E.D. The Role of Small Satellites in Our National Defence. In Proceedings of the Small Satellites Conference, "Market Drivers" Session, 1, 3rd Annual AIAA/USU Conference on Small Satellite, Logan, UT, USA, 26–28 September 1989. Available online: https://digitalcommons.usu.edu/cgi/viewcontent.cgi?article=2557&context=smallsat (accessed on 22 October 2021).
34. Keravala, J.; Lappas, V. Launching Small Spacecraft—The Surrey Space Centre Experience. In *The Space Transportation Market: Evolution or Revolution?* Rycroft, M., Ed.; Space Studies, 5; Springer: Dordrecht, The Netherlands, 2000. [CrossRef]
35. Choi, S.-D.; Kim, B.J.; Kim, E.E. An Introduction to the Kitsat program and the Activities at the Satrec in Korea. *COSPAR Coll.* **1999**, *10*, 9–16. [CrossRef]
36. Sun, W.; Sweeting, M.N.; Hodgart, M.S. Low earth orbit satellite communications experiments using the digital signal processing payload on the PoSAT-1 microsatellite. *Int. J. Satell. Commun.* **1995**, *13*, 485–502. [CrossRef]
37. Sweeting, M.N. Space at Surrey: Micro-mini-satellites for affordable access to space. *Air Space Eur.* **2000**, *2*, 38–52. [CrossRef]
38. da Silva Curiel, A.; Cawthorne, A.; Sweeting, M. Progress In Small Satellite Technology For Earth Observation Missions. In *Small Satellites for Earth Observation, Selected Proceedings of the 5th International Symposium of the International Academy of Astronautics, Berlin, Germany, 4–8 April 2005*; Röser, H.-P., Sandau, R., Valenzuela, A., Eds.; Walter de Gruyter: Berlin, Germany, 2005; pp. 50–63. [CrossRef]
39. Underwood, C.I.; Valenzuela, A.; Schoenherr, M.; Arancibia, M.; Fouquet, M. Initial in-orbit results from a low-cost atmospheric ozone monitor operating on board the FASat-Bravo microsatellite. *Phil. Trans. R. Soc. A* **2003**, *361*, 71–76. [CrossRef]
40. da Silva Curiel, A.; Boland, L.; Cooksley, J.; Bekhti, M.; Stephens, P.; Sun, W.; Sweeting, M.N. First results from the disaster monitoring constellation (DMC). *Acta Astronaut.* **2005**, *56*, 261–271. [CrossRef]
41. Stoll, E. The RapidEye constellation and its data products. In Proceedings of the 2012 IEEE Aerospace Conference, Big Sky, MT, USA, 3–10 March 2012; pp. 1–9.
42. Bhushan, S.; Shean, D.; Alexandrov, O.; Henderson, S. Automated digital elevation model (DEM) generation from very-high-resolution Planet SkySat triplet stereo and video imagery. *ISPRS J. Photogramm. Remote Sens.* **2021**, *173*, 151–165. [CrossRef]
43. eoPortal Directory of Space Missions. Available online: https://directory.eoportal.org/web/eoportal/satellite-missions (accessed on 22 October 2021).
44. Deepak, R.A.; Twiggs, R.J. Thinking Out of the Box: Space Science Beyond the CubSat. *J. Small Satell.* **2012**, *1*, 3–7.

45. Heidt, H.; Puig-Suari, J.; Moore, A.; Nakasuka, S.; Twiggs, R. CubeSat: A New Generation of Picosatellite for Education and Industry Low-Cost Space Experiment. In Proceedings of the 14th Annual AIAA/USU Conference on Small Satellite, Logan, UT, USA, 21–24 August 2000; p. 32.
46. Straub, J.; Korvald, C.; Nervold, A.; Mohammad, A.; Root, N.; Long, N.; Torgerson, D. OpenOrbiter: A Low-Cost, Educational Prototype CubeSat Mission Architecture. *Machines* **2013**, *1*, 1–32. [CrossRef]
47. Swarwout, M.; Kitts, C.; Twiggs, R.; Kenny, T.; Smith, B.R.; Lu, R.; Stattenfield, K.; Pranajaya, F. Mission results for Sapphire, a student-built satellite. *Acta Astronaut.* **2008**, *62*, 521–538. [CrossRef]
48. Puig-Suari, J.; Turner, C.; Ahlgren, W. Development of the standard CubeSat deployer and a CubeSat class PicoSatellite. In Proceedings of the 2001 IEEE Aerospace Conference, Big Sky, MT, USA, 10–17 March 2001; Volume 1, pp. 1/347–1/353. [CrossRef]
49. Puig-Suari, J.; Levegue, K.; Coelho, R.; Williams, S. Enabling Flexible Secondary Launches with the CubeSat Standar. In Proceedings of the 23rd Annual AIAA/USU Conference on Small Satellite, Logan, UT, USA, 10–13 August 2009; p. 61.
50. Aragon, B.; Ziliani, M.G.H.; Houborg, R.; Franz, T.E.; McCabe, M.F. CubeSats deliver new insights into agricultural water use at daily and 3 m resolutions. *Sci. Rep.* **2021**, *11*, 12131. [CrossRef]
51. Stephens, G.; Freeman, A.; Richard, E.; Pilewskie, P.; Larkin, P.; Chew, C.; Tanelli, S.; Brown, S.; Posselt, D.; Peral, E. The Emerging Technological Revolution in Earth Observations. *Bull. Am. Meteorol. Soc.* **2020**, *101*, E274–E285. [CrossRef]
52. Selva, D.; Krejci, D. A Survey and Assessment of the Capabilities of Cubesats for Earth Observation. *Acta Astronaut.* **2012**, *74*, 50–68. [CrossRef]
53. Toorian, A.; Diazm, K.; Lee, S. The CubeSat Approach to Space Access. In Proceedings of the 2008 IEEE Aerospace Conference, Big Sky, MT, USA, 1–8 March 2008; pp. 1–14. [CrossRef]
54. Wilkinson, K. From the Perspective of the Pioneers: The Small Sat Revolution. In Proceedings of the 20th Annual AIAA/USU Conference on Small Satellite, Logan, UT, USA, 14–17 August 2006; Volume 4.
55. Ferrari, F.; Franzese, V.; Pugliatti, M.; Giordano, C.; Topputo, F. Preliminary mission profile of HERA's Milani CubeSat. *Adv. Space Res.* **2021**, *67*, 2010–2029. [CrossRef]
56. eoPortal Directory of Earth Observations. Available online: https://earth.esa.int/web/eoportal/home (accessed on 22 October 2021).
57. Paek, S.W.; Balasubramanian, S.; Kim, S.; de Weck, O. Small-Satellite Synthetic Aperture Radar for Continuous Global Biospheric Monitoring: A Review. *Remote Sens.* **2020**, *12*, 2546. [CrossRef]
58. Capella Space. SAR Imagery Products Guide. 2020. 19p. Available online: https://vekom.com/wp-content/uploads/2020/12/Capella_Space_SAR_Imagery_Products_Guide.pdf (accessed on 22 October 2021).
59. Planet Labs.Planet Labs Specifications: Spacecraft Operations & Ground Systems. 2015. Available online: http://content.satimagingcorp.com.s3.amazonaws.com/media/pdf/Dove-PDF-Download (accessed on 22 October 2021).
60. Ignatenko, V.; Laurila, P.; Radius, A.; Lamentowski, L.; Antropov, O.; Muff, D. ICEYE Microsatellite SAR Constellation Status Update: Evaluation of First Commercial Imaging Modes. In Proceedings of the IEEE International Geoscience and Remote Sensing Symposium, Waikoloa, HI, USA, 26 September–2 October 2020; pp. 3581–3584. [CrossRef]
61. NASA. Ocean Surface Topography Mission/Jason 2 Launc, Press Kit. 2008. Available online: https://sealevel.jpl.nasa.gov/missions/ostm-jason-2/launch/ (accessed on 22 October 2021).
62. NASA; JPL; CNES; NOAA; EUMETSAT. JASON-3 Products Handbook, 2020; #SALP-MU-M-OP-16118-CN, Rev. 2.6. Available online: https://www.eumetsat.int/media/47149 (accessed on 22 October 2021).
63. Soldi, G.; Gaglione, D.; Forti, N.; Di Simone, A.; Daffinà, F.C.; Bottini, G.; Quattrociocchi, D.; Millefiori, L.M.; Braca, P.; Carniel, S.; et al. Space-Based Global Maritime Surveillance. Part I: Satellite Technologies. *IEEE Aerosp. Electron. Syst. Magaz.* **2021**, *36*, 8–28. [CrossRef]
64. Bastien-Thiry, C.; Bach, M.; Lifermann, A. PARASOL a Microsatellite in the A-Train for Earth Atmospheric Observations. In Proceedings of the 5th IAA Symposium on Small Satellites for Earth Observation, Paris, France, 4–8 April 2005.
65. Peral, E.; Tanelli, S.; Statham, S.; Joshi, S.; Imken, T.; Price, D.; Sauder, J.; Chahat, N.; Williams, A. RainCube: The first ever radar measurements from a CubeSat in space. *J. Appl. Remote Sens.* **2019**, *13*, 032504. [CrossRef]
66. RapidEye Website. Available online: https://earth.esa.int/eogateway/news/rapideye-constellation-retirement?te$\times$t=rapideye (accessed on 22 October 2021).
67. TEMPEST-D Website. Available online: https://esto.nasa.gov/wp-content/uploads/2020/07/Reising-TEMPEST-D.pdf (accessed on 22 October 2021).
68. Champagne, J.A.; Hansen, S.M.; Newswander, T.T. CubeSat Image Resolution Capabilities with Deployable Optics and Current Imaging Technology. In Proceedings of the 28th Annual AIAA/USU Conference on Small Satellite, Logan, UT, USA, 4–7 August 2014; p. 10.
69. Kurihara, J.; Takahashi, Y.; Sakamoto, Y.; Kuwahara, T.; Yoshida, K. HPT: A High Spatial Resolution Multispectral Sensor for Microsatellite Remote Sensing. *Sensors* **2018**, *18*, 619. [CrossRef] [PubMed]
70. Franceschetti, G.; Lanari, R. *Synthetic Aperture Radar Processing*; CRC Press: Boca Raton, FL, USA, 1999.
71. Roth, A.; Marschalk, U.; Winkler, K.; Schättler, B.; Huber, M.; Georg, I.; Künzer, C.; Dech, S. Years of Experience with Scientific TerraSAR-X Data Utilization. *Remote Sens.* **2018**, *10*, 1170. [CrossRef]
72. Young, N. Applications of Interferometric Synthetic Aperture Radar (InSAR): A Small Research Investigation. 2018. Available online: https://www.researchgate.net/publication/328773243_Applications_of_Interferometric_Synthetic_Aperture_Radar_InSAR_a_small_research_investigation (accessed on 11 October 2021).

73. Zalite, K.; Antropov, O.; Praks, J.; Voormansik, K.; Noorma, M. Monitoring of Agricultural Grasslands With Time Series of X-Band Repeat-Pass Interferometric SAR. *IEEE J. Sel. Top. Appl. Earth Obs. Remote Sens.* **2016**, *9*, 3687–3697. [CrossRef]
74. Paloscia, S.; Macelloni, G.; Santi, E.; Koike, T. A multifrequency algorithm for the retrieval of soil moisture on a large scale using microwave data from SMMR and SSM/I satellites. *IEEE Trans. Geosci. Remote Sens.* **2001**, *39*, 1655–1661. [CrossRef]
75. Chang, A.T.; Kelly, R.E.; Foster, J.L.; Hall, D.K. Global SWE monitoring using AMSR-E data. In Proceedings of the International Geoscience and Remote Sensing Symposium (IGARSS), Toulouse, France, 21–25 July 2003.
76. Le Vine, D.M.; Kao, M.; Tanner, A.B.; Swift, C.T.; Griffis, A. Initial results in the development of a synthetic aperture microwave radiometer. *IEEE Trans. Geosci. Remote Sens.* **1990**, *28*, 614–619. [CrossRef]
77. Le Vine, D.M. Synthetic Aperture Radiometer Systems. *IEEE Trans. Microw. Theory Tech.* **1999**, *47*, 2228–2236. [CrossRef]
78. Yang, X.; Yang, Z.; Yan, J.; Wu, L.; Jiang, M. Multi-Parameter Regularization Method for Synthetic Aperture Imaging Radiometers. *Remote Sens.* **2021**, *13*, 382. [CrossRef]
79. Alparone, M.; Nunziata, F.; Estatico, C.; Migliaccio, M. A multi-channel data fusion method to enhance the spatial resolution of microwave radiometer measurements. *IEEE Trans. Geosci. Remote Sens.* **2021**, *59*, 2213–2221. [CrossRef]
80. Lenti, F.; Nunziata, F.; Estatico, C.; Migliaccio, M. Spatial Resolution Enhancement of Earth Observation Products Using an Acceleration Technique for Iterative Methods. *IEEE Geosci. Remote Sens. Lett.* **2015**, *12*, 269–273. [CrossRef]
81. Long, D.G.; Brodzik, M.J.; Hardman, M.A. Enhanced-Resolution SMAP Brightness Temperature Image Products. *IEEE Trans. Geosci. Remote Sens.* **2019**, *57*, 4151–4163. [CrossRef]
82. CubeSat Design Specification (1U–12U), Rev. 14, CP–CDS–R14. The CubeSat Program, California State Polytechnic University; Retrieved January 18, 2022. p. 34. Available online: https://www.cubesat.org/ (accessed on 5 October 2021).
83. Hevner, R.; Holemans, W.; Puig-Suari, J.; Twiggs, R. An Advanced Standard for CubeSats. In Proceedings of the 25th Annual AIAA/USU Conference on Small Satellite, Logan, UT, USA, 8–11 August 2011; p. 15.
84. Peral, E.; Im, E.; Wye, L.; Lee, S.; Tanelli, S.; Rahmat-Samii, Y.; Horst, S.; Hoffman, J.; Yun, S.-H.; Imken, T.; et al. Radar Technologies for Earth Remote Sensing From CubeSat Platforms. *Proc. IEEE* **2018**, *106*, 404–418. [CrossRef]
85. Davoli, F.; Kourogiorgas, C.; Marchese, M.; Panagopoulos, A.; Patrone, F. Small satellites and CubeSats: Survey of structures, architectures, and protocols. *Int. J. Satell. Commun. Netw.* **2019**, *37*, 343–359. [CrossRef]
86. Nagel, G.W.; de Moraes Novo, E.M.L.; Kampel, M. Nanosatellites applied to optical Earth Observation: A review. *Rev. Ambient. Água* **2020**, *15*, e2513. [CrossRef]
87. Capaccioni, F.; Bellucci, G.; Rinaldi, G.; Saggin, B.; Valnegri, P.; Filacchione, G.; Della Corte, V.; Magrin, D.; Angarano, M.; Filippetto, D.; et al. DORA: Deployable Optics for Remote sensing Applications. *Eur. Sci. Congr.* **2020**, *14*, EPSC2020-1003.
88. Fernandez, L.; Sobrino, M.; Milian, O.; Aguilella, A.; Solanellas, A.; Badia, M.; Munoz-Martin, J.F.; Ruiz-de-Azua, J.A.; Sureda, M.; Camps, A. Deployment mechanism for a L-band helix antenna in 1-Unit Cubesat. *Acta Astronaut.* 2020; *in press*. [CrossRef]
89. Schlager, H.; Grewe, V.; Roiger, A. Chemical Composition of the Atmosphere. In *Atmospheric Physics, Research Topics in Aerospace*; Schumann, U., Ed.; Springer: Berlin/Heidelberg, Germany, 2012; p. 17. [CrossRef]
90. Isaksen, I.S.A.; Granier, C.; Myhre, G.; Berntsen, T.K.; Dalsøren, S.B.; Gauss, M.; Klimont, Z.; Benestad, R.; Bousquet, P.; Collins, W.; et al. Atmospheric composition change: Climate–Chemistry interactions. *Atmos. Environ.* **2009**, *43*, 5138–5192. [CrossRef]
91. LeGrande, A.; Tsigaridis, K.; Bauer, S.E. Role of atmospheric chemistry in the climate impacts of stratospheric volcanic injections. *Nat. Geosci.* **2016**, *9*, 652–655. [CrossRef]
92. Mylona, S. Sulphur dioxide emissions in Europe 1880–1991 and their effect on sulphur concentrations and depositions. *Tellus B* **1996**, *48*, 662–689. [CrossRef]
93. Liu, F.; Choi, S.; Li, C.; Fioletov, V.E.; McLinden, C.A.; Joiner, J.; Krotkov, N.A.; Bian, H.; Janssens-Maenhout, G.; Darmenov, A.-S.; et al. A new global anthropogenic $SO_2$ emission inventory for the last decade: A mosaic of satellite-derived and bottom-up emissions. *Atmos. Chem. Phys.* **2018**, *18*, 16571–16586. [CrossRef]
94. Clerbaux, C.; Hadji-Lazaro, J.; Turquety, S.; Mégie, G.; Coheur, P.F. Trace gas measurements from infrared satellite for chemistry and climate applications. *Atmos. Chem. Phys.* **2003**, *3*, 1495–1508. [CrossRef]
95. Clerbaux, C.; Boynard, A.; Clarisse, L.; George, M.; Hadji-Lazaro, J.; Herbin, H.; Hurtmans, J.; Pommier, M.; Razavi, A.; Turquety, S.; et al. Monitoring of atmospheric composition using the thermal infrared IASI/MetOp Sounder. *Atmos. Chem. Phys.* **2009**, *9*, 1495–1508. [CrossRef]
96. Riccio, A.; Giunta, G.; Landi, T.C.; Migliaccio, M. Remote optical observation of biomass burning: A feasibility and experimental case study with the SIM. GA hyperspectral system. *Int. J. Remote Sens.* **2011**, *32*, 6241–6259. [CrossRef]
97. Kuhn, J.; Bobrowski, N.; Lübcke, P.; Vogel, L.; Platt, U. A Fabry–Perot interferometer-based camera for two-dimensional mapping of $SO_2$ distributions. *Atmos. Meas. Tech.* **2014**, *7*, 3705–3715. [CrossRef]
98. Kuhn, J.; Platt, U.; Bobrowski, N.; Wagner, T. Towards imaging of atmospheric trace gases using Fabry–Pérot interferometer correlation spectroscopy in the UV and visible spectral range. *Atmos. Meas. Tech.* **2019**, *12*, 735–747. [CrossRef]
99. Fougnie, B.; Chimot, J.; Vàzquez-Navarro, M.; Marbach, T.; Bojkov, B. Aerosol retrieval from space—How does geometry of acquisition impact our ability to characterize aerosol properties. *J. Quant. Spectrosc. Radiat. Transf.* **2020**, *256*, 107304. [CrossRef]
100. Chiapello, I.; Formenti, P.; Mbemba Kabuiku, L.; Ducos, F.; Tanré, D.; Dublac, F. Aerosol optical properties derived from POLDER–3/PARASOL (2005–2013) over the Western Mediterranean Sea—Part 2: Spatial distribution and temporal variability. *Atmos. Chem. Phys.* **2021**, *21*, 12715–12737. [CrossRef]

101. Saari, H.; Näsilä, A.; Holmlund, C.; Mannila, R.; Näkki, I.; Ojanen, H.J.; Fussen, D.; Pieroux, D.; Demoulin, P.; Dekemper, E.; et al. Visible spectral imager for occultation and nightglow (VISION) for the PICASSO Mission. In Proceedings of the Sensors, Systems, and Next-Generation Satellites XIX, Toulouse, France, 21–24 September 2015; Volume 9639, p. 96391M. [CrossRef]
102. Barré, J.; Petetin, H.; Colette, A.; Guevara, M.; Peuch, V.-H.; Rouil, L.; Engelen, R.; Inness, A.; Flemming, J.; Pérez García-Pando, C.; et al. Estimating lockdown/induced European $NO_2$ changes using satellite and surface observations and air quality models. *Atmos. Chem. Phys.* **2021**, *21*, 7373–7394. [CrossRef]
103. Vîrghileanu, M.; Săvulescu, I.; Mihai, B.-A.; Nistor, C.; Dobre, R. Nitrogen Dioxide ($NO_2$) Pollution Monitoring with Sentinel-5P Satellite Imagery over Europe during the Coronavirus Pandemic Outbreak. *Remote Sens.* **2020**, *12*, 3575. [CrossRef]
104. Gupta, P.; Joiner, J.; Vasilkov, A.; Bhartia, P.K. Top-of-the-atmosphere shortwave flux estimation from satellite observations: An empirical neural network approach applied with data from the A–train constellation. *Atmos. Meas. Tech.* **2016**, *9*, 2813–2826. [CrossRef]
105. Munro, R.; Lang, R.; Klaes, D.; Poli, G.; Retscher, C.; Lindstrot, R.; Huckle, R.; Lacan, A.; Grzegorski, M.; Holdak, A.; et al. The GOME–2 instrument on the MetOp series of satellites: Instrument design, calibration, and level 1 data processing—An overview. *Atmos. Meas. Tech.* **2016**, *9*, 1279–1301. [CrossRef]
106. García, O.E.; Sepúlveda, E.; Schneider, M.; Hase, F.; August, T.; Blumenstock, T.; Kühl, S.; Munro, R.; Gómez-Peláez, Á.J.; Hultberg, T.; et al. Consistency and quality assessment of the MetOp–A/IASI and MetOp–B/IASI operational trace gas products ($O_3$, CO, $N_2O$, $CH_4$, and $CO_2$) in the subtropical North Atlantic. *Atmos. Meas. Tech.* **2016**, *9*, 2315–2333. [CrossRef]
107. Goldberg, M.D.; Kilcoyne, H.; Cikanek, H.; Mehta, A. Joint Polar Satellite System: The United States next generation civilian polar-orbiting environmental satellite system. *J. Geophys. Res. Atmos.* **2013**, *118*, 13463–13475. [CrossRef]
108. Pan, C.; Yan, B.; Flynn, L.; Beck, T.; Chen, J.; Huang, J. Recent Improvements to NOAA-20 Ozone Mapper Profiler Suite Nadir Profiler Sensor Data Records. In Proceedings of the 2021 IEEE International Geoscience and Remote Sensing Symposium IGARSS, Brussels, Belgium, 11–16 July 2021; pp. 7924–7926. [CrossRef]
109. Mannila, R.; Holmlund, C.; Ojanen, H.J.; Näsilä, A.; Saari, H. Short-wave infrared (SWIR) spectral imager based on Fabry-Perot interferometer for remote sensing. In Proceedings of the Sensors, Systems, and Next-Generation Satellites XVIII, Amsterdam, The Netherlands, 22–25 September 2014; Volume 9241, p. 92411M.
110. Rissanen, A.; Guo, B.; Saari, H.; Näsilä, A.; Mannila, R.; Akujärvi, A.; Ojanen, H. VTT's Fabry-Perot interferometer technologies for hyperspectral imaging and mobile sensing applications. In Proceedings of the MOEMS and Miniaturized Systems XVI, San Francisco, CA, USA, 28 January–2 February 2017; Volume 10116, p. 101160I. [CrossRef]
111. Erfan, M.; Sabry, Y.M.; Sakr, M.; Mortada, B.; Medhat, M.; Khalil, D. On-chip micro–electro–mechanical system Fourier transform infrared (MEMS FT-IR) spectrometer-based gas sensing. *Appl. Spectrosc.* **2016**, *70*, 897–904. [CrossRef] [PubMed]
112. Kita, D.M.; Miranda, B.; Favela, D.; Bono, D.; Michon, J.; Lin, H.; Gu, T.; Hu, J. High-performance and scalable on-chip digital Fourier transform spectroscopy. *Nat. Commun.* **2018**, *9*, 4405. [CrossRef]
113. Manzardo, O.; Herzig, H.P.; Marxer, C.R.; de Rooij, N.F. Miniaturized time-scanning Fourier transform spectrometer based on silicon technology. *Opt. Lett.* **1999**, *24*, 1705–1707. [CrossRef]
114. Nedeljkovic, M.; Velasco, A.V.; Khokhar, A.Z.; Delâge, A.; Cheben, P.; Mashanovich, G.Z. Mid-infrared silicon-on-insulator Fourier-transform spectrometer chip. *IEEE Photonics Technol. Lett.* **2016**, *28*, 528–531. [CrossRef]
115. Podmore, H.; Scott, A.; Cheben, P.; Velasco, A.V.; Schmid, J.H.; Vachon, M.; Lee, R. Demonstration of a compressive-sensing Fourier-transform on-chip spectrometer. *Opt. Lett.* **2017**, *42*, 1440–1443. [CrossRef] [PubMed]
116. Kern, S.; Spreen, G.; Kaleschke, L.; De La Rosa, S.; Heygster, G. Polynya signature simulation method polynya area in comparison to AMSR-E 89 GHz sea–ice concentrations in the Ross Sea and off the Adélie Coast, Antarctica, for 2002–05: First results. *Ann. Glaciol.* **2007**, *46*, 409–418. [CrossRef]
117. Parmiggiani, F. Fluctuations of Terra Nova Bay polynya as observed by active (ASAR) and passive (AMSR-E) microwave radiometers. *Int. J. Remote Sens.* **2006**, *27*, 2459–2467. [CrossRef]
118. Morales Maqueda, M.Á.; Willmott, A.J.; Biggs, N.R.T. Polynya dynamics: A review of observations and modeling. *Rev. Geophys.* **2004**, *42*, RG1004. [CrossRef]
119. Martin, S. Polynyas. In *Encyclopedia of Ocean Sciences*, 3rd ed.; Collection: Earth Systems and Environmental Sciences; Academic Press: Cambridge, MA, USA, 2019; Volume 6, pp. 175–180. [CrossRef]
120. Sansiviero, M.; Morales Maqueda, M.Á.; Fusco, G.; Aulicino, G.; Flocco, D.; Budillon, G. Modelling sea ice formation in the Terra Nova Bay polynya. *J. Mar. Syst.* **2017**, *166*, 4–25. [CrossRef]
121. Vincent, R.F. A Study of the North Water Polynya Ice Arch using Four Decades of Satellite Data. *Sci. Rep.* **2019**, *9*, 20278. [CrossRef] [PubMed]
122. Jena, B.; Ravichandran, M.; Turner, J. Recent reoccurrence of large open-ocean polynya on the Maud Rise seamount. *Geophys. Res. Lett.* **2019**, *46*, 4320–4329. [CrossRef]
123. Stewart, C.L.; Christoffersen, P.; Nicholls, K.W.; Williams, M.J.M.; Dowdeswell, J.A. Basal melting of Ross Ice Shelf from solar heat absorption in an ice-front polynya. *Nat. Geosci.* **2019**, *12*, 435–440. [CrossRef]
124. Hollands, T.; Dierking, W. Dynamics of the Terra Nova Bay Polynya: The potential of multi-sensor satellite observations. *Remot. Sens. Environ.* **2016**, *187*, 30–48. [CrossRef]
125. Paul, S.; Willmes, S.; Heinemann, G. Long-term coastal-polynya dynamics in the southern Weddell Sea from MODIS thermal-infrared imagery. *Cryosphere* **2015**, *9*, 2027–2041. [CrossRef]

126. Naftaly, U.; Levy-Nathansohn, R. Overview of the TECSAR Satellite Hardware and Mosaic Mode. *IEEE Geosci. Remote Sens. Lett.* **2008**, *5*, 423–426. [CrossRef]
127. Suwaidi, A.A. DubaiSat–2 mission overview. In Proceedings of the Sensors, Systems, and Next-Generation Satellites XVI, Edinburgh, UK, 24–27 September 2012; Volume 8533, p. 85330W. [CrossRef]
128. Cheng, Z.; Pang, X.; Zhao, X.; Tan, C. Spatio-temporal variability and model parameter sensitivity analysis of ice production in Ross Ice Shelf Polynya from 2003 to 2015. *Remote Sens.* **2017**, *9*, 934. [CrossRef]
129. Safyan, M. Planet's Dove Satellite Constellation. In *Handbook of Small Satellites*; Pelton, J., Ed.; Springer: Cham, Switzerland, 2020. [CrossRef]
130. Tyc, G.; Tulip, J.; Schulten, D.; Krischke, M.; Oxfort, M. The RapidEye mission design. *Acta Astron.* **2005**, *56*, 213–219. [CrossRef]
131. Aulicino, G.; Sansiviero, M.; Paul, S.; Cesarano, C.; Fusco, G.; Wadhams, P.; Budillon, G. A New Approach for Monitoring the Terra Nova Bay Polynya through MODIS Ice Surface Temperature Imagery and Its Validation during 2010 and 2011 Winter Seasons. *Remote Sens.* **2018**, *10*, 366. [CrossRef]
132. Willmes, S.; Krumpen, T.; Adams, S.; Rabenstein, L.; Haas, C.; Hoelemann, J.; Hendricks, S.; Heinemann, G. Cross-validation of polynya monitoring methods from multisensor satellite and airborne data: A cases study for the Laptev Sea. Can. *J. Remote Sens.* **2010**, *36*, S196–S210. [CrossRef]
133. Ciappa, A.; Budillon, G. The Terra Nova Bay (Antarctica) polynya observed by MODIS ice surface temperature imagery from May to June 2009. *Int. J. Remote Sens.* **2012**, *33*, 4567–4582. [CrossRef]
134. Key, J.R.; Collins, J.B.; Fowler, C.; Stone, R.S. High-latitude surface temperature estimates from thermal satellite data. *Remote Sens. Environ.* **1997**, *61*, 302–309. [CrossRef]
135. Fortescue, P.; Stark, J.; Swinerd, G. *Spacecraft Systems Engineering*, 4th ed.; Wiley: Hoboken, NJ, USA, 2011.
136. Artigas, M.L.; Llebot, C.; Ross, O.N.; Neszi, N.Z.; Rodellas, V.; Garcia-Orellana, J.; Masqué, P.; Piera, J.; Estrada, M.; Berdalet, E. Understanding the spatio-temporal variability of phytoplankton biomass distribution in a microtidal Mediterranean estuary. *Deep. Sea Res. Part II Top. Stud. Oceanogr.* **2014**, *101*, 180–192. [CrossRef]
137. Madricardo, F.; Foglini, F.; Campiani, E.; Grande, V.; Catenacci, E.; Petrizzo, A.; Kruss, A.; Toso, C.; Trincardi, F. Assessing the human footprint on the sea-floor of coastal systems: The case of the Venice Lagoon, Italy. *Sci. Rep.* **2019**, *9*, 6615. [CrossRef]
138. Melet, A.; Teatini, P.; Le Cozannet, G.; Jamet, C.; Conversi, A.; Benveniste, J.; Almar, R. Earth Observations for Monitoring Marine Coastal Hazards and Their Drivers. *Surv. Geophys.* **2020**, *41*, 1489–1534. [CrossRef]
139. Robinson, S. *Measuring the Oceans from Space: The Principles and Methods of Satellite Oceanography*, 1st ed.; Springer: Berlin/Heidelberg, Germany; New York, NY, USA, 2004.
140. Ardhuin, F.; Stopa, J.E.; Chapron, B.; Collard, F.; Husson, R.; Jensen, R.E.; Johannessen, J.; Mouche, A.; Passaro, M.; Quartly, G.D.; et al. Observing Sea States. *Front. Mar. Sci.* **2019**, *6*, 124. [CrossRef]
141. Cipollini, P.; Benveniste, J.; Birol, F.; Fernandes, M.; Obligis, E.; Passaro, M.; Strub, P.T.; Valladeau, G.; Vignudelli, S.; Wilkin, J. Satellite altimetry in coastal regions. In *Satellite Altimetry over Oceans and Land Surfaces Earth Observation of Global Changes Book Series*; Stammer, D., Cazenave, A., Eds.; CRC Press: New York, NY, USA, 2017; pp. 343–380.
142. Collard, F.; Ardhuin, F.; Chapron, B. Extraction of coastal ocean wave fields from SAR images. *IEEE J. Ocean. Eng.* **2005**, *30*, 526–533. [CrossRef]
143. Passaro, M.; Fenoglio-Marc, L.; Cipollini, P. Validation of significant wave height from improved satellite altimetry in the German Bight. *IEEE Trans. Geosci. Remote Sens.* **2015**, *53*, 2146–2156. [CrossRef]
144. Behrenfeld, M.J.; O'Malley, R.T.; Siegel, D.A.; McClain, C.R.; Sarmiento, J.L.; Feldman, G.C.; Milligan, A.J.; Falkowski, P.G.; Letelier, R.M.; Boss, E.S. Climate-driven trends in contemporary ocean productivity. *Nature* **2006**, *444*, 752–755. [CrossRef] [PubMed]
145. Groom, S.; Sathyendranath, S.; Ban, Y.; Bernard, S.; Brewin, R.; Brotas, V.; Brockmann, C.; Chauhan, P.; Choi, J.-K.; Chuprin, A.; et al. Satellite Ocean Colour: Current Status and Future Perspective. *Front. Mar. Sci.* **2019**, *6*, 485. [CrossRef]
146. Wernand, M.R.; van der Woerd, H.J.; Gieskes, W.W.C. Trends in Ocean Colour and Chlorophyll Concentration from 1889 to 2000, Worldwide. *PLoS ONE* **2010**, *8*, e63766. [CrossRef] [PubMed]
147. Zielinski, O.; Busch, J.A.; Cembella, A.D.; Daly, K.L.; Engelbrektsson, J.; Hannides, A.K.; Schmidt, H. Detecting marine hazardous substances and organisms: Sensors for pollutants, toxins, and pathogens. *Ocean Sci.* **2009**, *5*, 329–349. [CrossRef]
148. Bunt, J.S. Primary Productivity of Marine Ecosystems. In *Primary Productivity of the Biosphere. Ecological Studies (Analysis and Synthesis)*; Lieth, H., Whittaker, R.H., Eds.; Springer: Berlin/Heidelberg, Germany, 1975; Volume 14. [CrossRef]
149. Lévy, M.; Franks, P.J.S.; Smith, K.S. The role of submesoscale currents in structuring marine ecosystems. *Nat. Commum.* **2018**, *9*, 4758. [CrossRef]
150. Mahadevan, A. The Impact of Submesoscale Physics on Primary Productivity of Plankton. *Annu. Rev. Mar. Sci.* **2016**, *8*, 161–184. [CrossRef]
151. Molinero, J.C.; Ibanez, F.; Souissi, S.; Bosc, E.; Nival, P. Surface patterns of zooplankton spatial variability detected by high frequency sampling in the NW Mediterranean. Role of density fronts. *J. Mar. Syst.* **2008**, *69*, 271–282. [CrossRef]
152. Ramírez, T.; Muñoz, M.; Reul, A.; García-Martínez, M.C.; Moya, F.; Vargas-Yáñez, M.; Bautista, B. The Biogeochemical Context of Marine Planktonic Ecosystems. In *Alboran Sea—Ecosystems and Marine Resources*; Báez, J.C., Vázquez, J.T., Camiñas, J.A., Malouli Idrissi, M., Eds.; Springer: Cham, Switzerland, 2021. [CrossRef]
153. Bini, M.; Rossi, V. Climate Change and Anthropogenic Impact on Coastal Environments. *Water* **2021**, *13*, 1182. [CrossRef]

154. De Maio, A.; Moretti, M.; Sansone, E.; Spezie, G.; Vultaggio, M. Outline of marine currents in the bay of Naples and some considerations on pollutant transport. *Il Nuovo Cim. C* **1985**, *8*, 955–969. [CrossRef]
155. Schueler, C.; Holmes, A. SeaHawk CubeSat system engineering. In Proceedings of the Remote Sensing System Engineering VI, San Diego, CA, USA, 28 August–1 September 2016; Volume 9977, p. 99770A. [CrossRef]
156. Mhangara, P. The Emerging Role of Cubesats for Earth Observation Applications in South Africa. *Photogramm. Eng. Remote Sens.* **2020**, *86*, 333–340. [CrossRef]
157. Artale, V.; Iudicone, D.; Santoleri, R.; Rupolo, V.; Marullo, S.; D'Ortenzio, F. Role of surface fluxes in ocean general circulation models using satellite sea surface temperature: Validation of and sensitivity to the forcing frequency of the Mediterranean thermohaline circulation. *J. Geophys. Res.* **2002**, *107*, 3120. [CrossRef]
158. O'Carroll, A.G.; Armstrong, E.M.; Beggs, H.M.; Bouali, M.; Casey, K.S.; Corlett, G.K.; Dash, P.; Donlon, C.J.; Gentemann, C.L.; Høyer, J.L.; et al. Observational Needs of Sea Surface Temperature. *Front. Mar. Sci.* **2019**, *6*, 420. [CrossRef]
159. López García, M.J. SST Comparison of AVHRR and MODIS Time Series in the Western Mediterranean Sea. *Remote Sens.* **2020**, *12*, 2241. [CrossRef]
160. Chelton, D.B.; Wentz, F.J. Global Microwave Satellite Observations of Sea Surface Temperature for Mumerical Weather Prediction and Climate Research. *Am. Meteorol. Soc.* **2005**, *86*, 1097–1116. [CrossRef]
161. Wentz, F.J.; Gentemann, C.; Smith, D.; Chelton, D. Satellite measurements of sea surface temperature through clouds. *Science* **2000**, *288*, 847–850. [CrossRef] [PubMed]
162. Boutin, J.; Reul, N.; Koehler, J.; Martin, A.; Catany, R.; Guimbard, S.; Rouffi, F.; Vergely, J.L.; Arias, M.; Chakroun, M.; et al. Satellite-based sea surface salinity designed for ocean and climate studies. *J. Geophys. Res. Oceans* **2021**, *126*, e2021JC017676. [CrossRef]
163. Liu, C.; Liang, X.; Ponte, R.M.; Vinogradova, N.; Wang, O. Vertical redistribution of salt and layered changes in global ocean salinity. *Nat. Commun.* **2019**, *10*, 3445. [CrossRef]
164. Bao, S.; Wang, H.; Zhang, R.; Yan, H.; Chen, J. Comparison of satellite-derived sea surface salinity products from SMOS, Aquarius, and SMAP. *J. Geophys. Res. Oceans* **2019**, *124*, 1932–1944. [CrossRef]
165. Yu, L.; Josey, S.A.; Bingham, F.M.; Lee, T. Intensification of the global water cycle and evidence from ocean salinity: A synthesis review. *Ann. N. Y. Acad. Sci.* **2020**, *1472*, 76–94. [CrossRef]
166. Reul, N.; Grodsky, S.A.; Arias, M.; Boutin, J.; Catany, R.; Chapron, B.; D'Amico, F.; Dinnat, E.; Donlon, C.; Fore, A.; et al. Sea surface salinity estimates from spaceborne L-band radiometers: An overview of the first decade of observation (2010–2019). *Remote Sens. Environ.* **2020**, *242*, 111769. [CrossRef]
167. Font, J.; Camps, A.; Borges, A.; Martín-Neira, M.; Boutin, J.; Reul, N.; Kerr, Y.H.; Hahne, A.; Mecklenburg, S. SMOS: The Challenging Sea Surface Salinity Measurement from Space. *Proc. IEEE* **2010**, *98*, 649–665. [CrossRef]
168. Chelton, D.B.; Schlax, M.G. The Accuracies of Smoothed Sea Surface Height Fields Constructed from Tandem Satellite Altimeter Datasets. *J. Atmos. Oceanic. Tech.* **2003**, *20*, 1276–1302. [CrossRef]
169. Woodworth, P.L.; Melet, A.; Marcos, M.; Ray, R.D.; Wöppelmann, G.; Sasaki, Y.N.; Cirano, M.; Hibbert, A.; Huthance, J.M.; Monserrat, S.; et al. Forcing Factors Affecting Sea Level Changes at the Coast. *Surv. Geophys.* **2019**, *40*, 1351–1397. [CrossRef]
170. Klemas, V.; Yan, X.-H. Subsurface and deeper ocean remote sensing from satellites: An overview and new results. *Prog. Oceanogr.* **2014**, *122*, 1–9. [CrossRef]
171. Salameh, E.; Frappart, F.; Marieu, V.; Spodar, A.; Parisot, J.-P.; Hanquiez, V.; Turki, I.; Laignel, B. Monitoring Sea Level and Topography of Coastal Lagoons Using Satellite Radar Altimetry: The Example of the Arcachon Bay in the Bay of Biscay. *Remote Sens.* **2018**, *10*, 297. [CrossRef]
172. Hersbach, H.; Stoffelen, A.; de Haan, S. An improved C-band scatterometer ocean geophysical model function: CMOD5. *J. Geophys. Res. Oceans* **2007**, *112*, 1–18. [CrossRef]
173. Zhang, L.; Shi, H.; Wang, Z.; Yu, H.; Yin, X.; Liao, Q. Comparison of Wind Speeds from Spaceborne Microwave Radiometers with In Situ Observations and ECMWF Data over the Global Ocean. *Remote Sens.* **2018**, *10*, 425. [CrossRef]
174. Lin, H.; Xu, Q.; Zheng, Q. An overview on SAR measurements of sea surface wind. *Progress Nat. Sci.* **2008**, *18*, 913–919. [CrossRef]
175. Corcione, V.; Grieco, G.; Portabella, M.; Nunziata, F.; Migliaccio, M. A novel azimuth cutoff implementation to retrieve sea surface wind speed from SAR imagery. *IEEE Trans. Geosci. Remote Sens.* **2018**, *57*, 3331–3340. [CrossRef]
176. Ho, C.-R.; Zheng, Q.; Soong, Y.S.; Kuo, N.-J.; Hu, J.-H. Seasonal variability of sea surface height in the South China Sea observed with TOPEX/Poseidon altimeter data. *J. Geophys. Res.* **2000**, *105*, 13981–13990. [CrossRef]
177. Dufau, C.; Orsztynowicz, M.; Dibarboure, G.; Morrow, R.; Le Traon, P.-Y. Mesoscale resolution capability of altimetry: Present and future. *J. Geophys. Res. Oceans* **2016**, *121*, 4910–4927. [CrossRef]
178. Quartly, G.D.; Smith, W.H.F.; Passaro, M. Removing Intra-1-Hz Covariant Error to Improve Altimetric Profiles of σ0 and Sea Surface Height. *IEEE Trans. Geosci. Remote Sens.* **2019**, *57*, 3741–3752. [CrossRef]
179. Chelton, D.B.; Ries, J.C.; Haines, B.J.; Fu, L.-L.; Callahan, P.S. Satellite altimetry. In *Satellite Altimetry and Earth Science: A Handbook of Techniques and Applications 69, International Geophysics Series*; Fu, L.-L., Cazenave, A., Eds.; Academic Press: Cambridge, MA, USA, 2001; pp. 1–131.
180. Deng, X.; Featherstone, W.E. A coastal retracking system for satellite radar altimeter waveforms: Application to ERS-2 around Australia. *J. Geophys. Res.* **2005**, *111*, C06012. [CrossRef]

181. Passaro, M.; Cipollini, P.; Vignudelli, S.; Quartly, G.D.; Snaith, H.M. ALES: A multi-mission adaptive subwaveform retracker for coastal and open ocean altimetry. *Remote Sens. Environ.* **2014**, *145*, 173–189. [CrossRef]
182. Bannoura, W.J.; Wade, A.; Srinivas, D.N. NOAA Ocean Surface Topography Mission Jason-2 project overview. In Proceedings of the OCEANS 2005 MTS/IEEE, Washington, DC, USA, 17–23 September 2005; Volume 3, pp. 2155–2159. [CrossRef]
183. Scharroo, R.; Bonekamp, H.; Ponsard, C.; Parisot, F.; von Engeln, A.; Tahtadjiev, M.; de Vriendt, K.; Montagner, F. Jason continuity of services: Continuing the Jason altimeter data records as Copernicus Sentinel-6. *Ocean Sci.* **2016**, *12*, 471–479. [CrossRef]
184. Donlon, C.J.; Cullen, R.; Giulicchi, L.; Vuilleumier, P.; Francis, C.R.; Kuschnerus, M.; Simpson, W.; Bouridah, A.; Caleno, M.; Bertoni, R.; et al. The Copernicus Sentinel-6 mission: Enhanced continuity of satellite sea level measurements from space. *Remote Sens. Environ.* **2021**, *258*, 112395. [CrossRef]
185. Lowe, S.T.; Zuffada, C.; Chao, Y.; Kroger, P.; Young, L.E.; LaBrecque, J.L. 5-cm-Precision aircraft ocean altimetry using GPS reflections. *Geophys. Res. Lett.* **2002**, *29*, 13-1–13-4. [CrossRef]
186. Clarizia, M.P.; Ruf, C.; Cipollini, P.; Zuffada, C. First spaceborne observation of sea surface height using GPS-Reflectometry. *Geophys. Res. Lett.* **2016**, *43*, 767–774. [CrossRef]
187. Martin-Neira, M. A Passive Reflectometry and Interferometry System (PARIS): Application to ocean altimetry. *ESA J.* **1993**, *17*, 331–355.
188. Martin-Neira, M.; D'Addio, S.; Buck, C.; Floury, N.; Prieto-Cerdeira, R. The PARIS ocean altimeter in-orbit demonstrator. *IEEE Trans. Geosci. Remote Sens.* **2011**, *49*, 2209–2237. [CrossRef]
189. Boudouresque, C.F.; Bernard, G.; Bonhomme, P.; Charbonnel, E.; Diviacco, G.; Meinesz, A.; Pergent, G.; Pergent-Martini, C.; Ruitton, S.; Tunesi, L. *Protection and Conservation of Posidonia oceanica Meadows*; RAMOGE and RAC/SPA Publisher: Tunis, Tunisia, 2012.
190. Buhl-Mortensen, L.; Vanreusel, A.; Gooday, A.J.; Levin, L.A.; Priede, I.G.; Buhl-Mortensen, P.; Gheerardyn, H.; King, N.J.; Raes, M. Biological structures as a source of habitat heterogeneity and biodiversity on the deep ocean margins. *Mar. Ecol.* **2010**, *31*, 21–50. [CrossRef]
191. Buonocore, E.; Donnarumma, L.; Appolloni, L.; Miccio, A.; Russo, G.F.; Franzese, P.P. Marine natural capital and ecosystem services: An environmental accounting model. *Ecol. Modell.* **2020**, *424*, 109029. [CrossRef]
192. Costanza, R.; d'Arge, R.; de Groot, R.; Farber, S.; Grasso, M.; Hannon, B.; Limburg, K.; Naeem, S.; O'Neill, R.V.; Paruelo, J.; et al. The value of the world's ecosystem services and natural capital. *Nature* **1997**, *387*, 253–260. [CrossRef]
193. Hemminga, M.A.; Duarte, C.M. *Seagrass Ecology*; Cambridge University Press: Cambridge, UK, 2000. [CrossRef]
194. Mazarrasa, I.; Samper-Villarreal, J.; Serrano, O.; Lavery, P.S.; Lovelock, C.E.; Marbà, N.; Duarte, C.M.; Cortés, J. Habitat characteristics provide insights of carbon storage in seagrass meadows. *Mar. Pollut. Bull.* **2018**, *134*, 106–117. [CrossRef]
195. Akçalı, B.; Taşkın, E.; Kaman, G.; Evcen, A.; Çalık, H.; Akyol, O. Posidonia Oceanica Monitoring System on the Coast of Aegean Sea of Turkey. In *Eighth International Symposium "Monitoring of Mediterranean Coastal Areas. Problems and Measurement Techniques"*; Bonora, L., Carboni, D., De Vincenzi, M., Eds.; Firenze University Press: Florence, Italy, 2000; pp. 475–482. [CrossRef]
196. Buia, M.C.; Gambi, M.C.; Dappiano, M. The seagrass ecosystems. In *Mediterranean Marine Benthos: A Manual for Its Sampling and Study, Biologia Marina Mediterranea*; Gambi, M.C., Dappiano, M., Eds.; Società Italiana di Biologia Marina: Genoa, Italy, 2004; Volume 11, (Suppl. 1), pp. 133–183.
197. Franzese, P.P.; Buonocore, E.; Paoli, C.; Massa, F.; Donati, S.; Fanciulli, G.; Miccio, A.; Mollica, E.; Navone, A.; Russo, G.F.; et al. Environmental Accounting in Marine Protected Areas: The EAMPA Project. *J. Environ. Account. Manag.* **2015**, *3*, 324–332. [CrossRef]
198. Orth, R.J.; Carruthers, T.J.B.; Dennison, W.C.; Duarte, C.M.; Fourqurean, J.W.; Heck, K.L.; Hughes, A.R.; Kendrick, G.A.; Kenworthy, W.J.; Olyarnik, S.; et al. A Global Crisis for Seagrass Ecosystems. *Bioscience* **2006**, *56*, 987. [CrossRef]
199. Wright, J.P.; Jones, C.G. The Concept of Organisms as Ecosystem Engineers Ten Year On: Progress, Limitations, and Challenges. *BioScience* **2006**, *56*, 203–209. [CrossRef]
200. Roelfsema, C.M.; Lyons, M.; Kovacs, E.M.; Maxwell, P.; Saunders, M.I.; Samper-Villarreal, J.; Phinn, S.R. Multi-temporal mapping of seagrass cover, species and biomass: A semi-automated object based image analysis approach. *Remote Sens. Environ.* **2014**, *150*, 172–187. [CrossRef]
201. Traganos, D.; Reinartz, P. Interannual Change Detection of Mediterranean Seagrasses Using RapidEye Image Time Series. *Front. Plant Sci.* **2018**, *9*, 96. [CrossRef]
202. Mateo, M.-Á.; Sánchez-Lizaso, J.-L.; Romero, J. *Posidonia oceanica* "banquettes": A preliminary assessment of the relevance for meadow carbon and nutrients budget. *Estuar. Coast. Shelf Sci.* **2003**, *56*, 85–90. [CrossRef]
203. Nellemann, C.; Corcoran, E.; Duarte, C.M.; Valdés, L.; De Young, C.; Fonseca, L.; Grimsditch, G. (Eds.) Blue Carbon. In *A Rapid Response Assessment*; GRID-Arendal; United Nations Environment Programme: Nairobi, Kenya, 2009; Available online: www.grida.no (accessed on 8 October 2021).
204. Carruthers, T.J.B.; Dennison, W.C.; Kendrick, G.A.; Waycott, M. Seagrasses of south—West Australia: A conceptual synthesis of the world's most diverse and extensive seagrass meadows. *J. Exp. Mar. Biol. Ecol.* **2007**, *350*, 21–45. [CrossRef]
205. Telesca, L.; Belluscio, A.; Criscoli, A.; Ardizzone, G.; Apostolaki, E.T.; Fraschetti, S.; Gristina, M.; Knittweis, L.; Martin, C.S.; Pergent, G.; et al. Seagrass meadows (*Posidonia oceanica*) distribution and trajectories of change. *Sci. Rep.* **2015**, *5*, 1–14. [CrossRef] [PubMed]

206. Short, F.T.; Polidoro, B.; Livingstone, S.R.; Carpenter, K.E.; Bandeira, S.; Bujang, J.S.; Calumpong, H.P.; Carruthers, T.J.B.; Coles, R.G.; Dennison, W.C.; et al. Extinction risk assessment of the world's seagrass species. *Biol. Conserv.* **2011**, *144*, 1961–1971. [CrossRef]
207. Waycott, M.; Duarte, C.M.; Carruthers, T.J.B.; Orth, R.J.; Dennison, W.C.; Olyarnik, S.; Calladine, A.; Fourqurean, J.W.; Heck, K.L.; Hughes, A.R.; et al. Accelerating loss of seagrasses across the globe threatens coastal ecosystems. *Proc. Natl. Acad. Sci. USA* **2009**, *106*, 12377–12381. [CrossRef] [PubMed]
208. Ruiz, J.M.; Pérez, M.; Romero, J. Effects of Fish Farm Loadings on Seagrass (*Posidonia oceanica*) Distribution, Growth and Photosynthesis. *Mar. Pollut. Bull.* **2001**, *42*, 749–760. [CrossRef]
209. Häyhä, T.; Franzese, P.P. Ecosystem services assessment: A review under an ecological-economic and systems perspective. *Ecol. Modell.* **2014**, *289*, 124–132. [CrossRef]
210. Franzese, P.P.; Buonocore, E.; Donnarumma, L.; Russo, G.F. Natural capital accounting in marine protected areas: The case of the Islands of Ventotene and S. Stefano (Central Italy). *Ecol. Modell.* **2017**, *360*, 290–299. [CrossRef]
211. Appolloni, L.; Buonocore, E.; Russo, G.F.; Franzese, P.P. The use of remote sensing for monitoring *Posidonia oceanica* and Marine Protected Areas: A systemic review. *Ecol. Quest.* **2020**, *1*, 7–17. [CrossRef]
212. Cozza, R.; Rende, F.; Ferrari, M.; Bruno, L.; Pacenza, M.; Dattola, L.; Bitonti, M.B. Biomonitoring of *Posidonia oceanica* beds by a multiscale approach. *Aquat. Bot.* **2019**, *156*, 14–24. [CrossRef]
213. Phinn, S.; Roelfsema, C.; Kovacs, E.; Canto, R.; Lyons, M.; Saunders, M.; Maxwell, P. Mapping, monitoring and modelling seagrass using remote sensing techniques. In *Seagrasses of Australia*; Larkum, A.W.D., Kendrick, G.A., Ralph, P.J., Eds.; Springer: Berlin/Heidelberg, Germany, 2018; pp. 445–487. [CrossRef]
214. Veettil, B.K.; Ward, R.D.; Lima, M.D.A.C.; Stankovic, M.; Hoai, P.N.; Quang, N.X. Opportnities for seagrass research derived from remote sensing: A review of current methods. *Ecol. Indic.* **2020**, *117*, 106560. [CrossRef]
215. Giardino, C.; Bartoli, M.; Candianai, G.; Bresciani, M.; Pellegrini, L. Recent changes in macrophyte colonisation patterns: An imaging spectrometry-based evaluation of southern Lake Garda (northern Italy). *J. Appl. Remote Sens.* **2007**, *1*, 11509. [CrossRef]
216. Catucci, E.; Scardi, M. A Machine Learning approach to the assessment of the vulnerability of *Posidonia oceanica* meadows. *Ecol. Indic.* **2020**, *108*, 105744. [CrossRef]
217. Pham, T.D.; Xia, J.; Ha, N.T.; Bui, D.T.; Le, N.N.; Takeuchi, W. A Review of Remote Sensing Approaches for Monitoring Blue Carbon Ecosystems: Mangroves, Seagrasses and Salt Marshes during 2010–2018. *Sensors* **2019**, *19*, 1933. [CrossRef] [PubMed]
218. Thessen, A.E. Adoption of machine learning techniques in ecology and earth science. *One Ecosyst.* **2016**, *1*, 1–38. [CrossRef]
219. Pasqualini, V.; Pergent-Martini, C.; Pergent, G.; Agreil, M.; Skoufas, G.; Sourbes, L.; Tsirika, A. Use of SPOT 5 for mapping seagrasses: An application to *Posidonia oceanica*. *Remote Sens. Environ.* **2005**, *94*, 39–45. [CrossRef]
220. Maglione, P. Very High Resolution Optical Satellites: An Overview of the Most Commonly used. *Am. J. Appl. Sci.* **2016**, *13*, 91–99. [CrossRef]
221. Rende, S.F.; Bosman, A.; Di Mento, R.; Bruno, F.; Lagudi, A.; Irving, A.D.; Dattola, L.; Giambattista, L.D.; Lanera, P.; Proietti, R.; et al. Ultra-High-Resolution Mapping of *Posidonia oceanica* (L.) Delile Meadows through Acoustic, Optical Data and Object-based Image Classification. *J. Mar. Sci. Eng.* **2020**, *8*, 647. [CrossRef]
222. Coffer, M.M.; Schaeffer, B.A.; Zimmerman, R.C.; Hill, V.; Li, J.; Islam, K.A.; Whitman, P.J. Performance across WorldView-2 and RapidEye for reproducuble seagrass mapping. *Remote Sens. Environ.* **2020**, *250*, 112036. [CrossRef]
223. Fornes, A.; Basterretxea, G.; Orfila, A.; Jordi, A.; Alvarez, A.; Tintore, J. Mapping *Posidonica oceanica* from IKONOS. *ISPRS J. Photogramm.* **2006**, *60*, 315–322. [CrossRef]
224. Giardino, C.; Bresciani, M.; Fava, F.; Matta, E.; Brando, V.E.; Colombo, R. Mapping Submerged Habitats and Mangroves of Lampi Island Marine National Park (Myanmar) from in Situ and Satellite Observations. *Remote Sens.* **2016**, *8*, 2. [CrossRef]
225. Matta, E.; Aiello, M.; Bresciani, M.; Gianinetto, M.; Musanti, M.; Giardino, C. Mapping Posidonia meadow from high spatial resolution images in the Gulf of Oristano (Italy). In Proceedings of the 2014 IEEE Geoscience and Remote Sensing Symposium, Quebec City, QC, Canada, 13–18 July 2014; pp. 5152–5155. [CrossRef]
226. Giorgi, F. Climate change hot spots. *Geophys. Res. Lett.* **2006**, *33*, L08707. [CrossRef]
227. Alexander, L.V.; Zhang, X.; Peterson, T.C.; Caesar, J.; Gleason, B.; Klein Tank, A.M.G.; Haylock, M.; Collins, D.; Trewin, B.; Rahimzadeh, F.; et al. Global observed changes in daily climate extremes of temperature and precipitation. *J. Geophys. Res.* **2006**, *111*, D05109. [CrossRef]
228. Bucchignani, E.; Montesarchio, M.; Zollo, A.L.; Mercogliano, P. High-resolution climate simulations with COSMO-CLM over Italy: Performance evaluation and climate projections for the XXI century. *Int. J. Climatol.* **2015**, *36*, 735–756. [CrossRef]
229. Donat, M.G.; Alexander, L.V.; Yang, H.; Durre, I.; Vose, R.; Dunn, R.J.H.; Willett, K.M.; Aguilar, E.; Brunet, M.; Caesar, J.; et al. Updated analyses of temperature and precipitation extreme indices since the beginning of the twentieth century: The HadEX2 dataset. *J. Geophys. Res.* **2013**, *118*, 2098–2118. [CrossRef]
230. Cardell, M.F.; Amengual, A.; Romero, R.; Ramis, C. Future extremes of temperature and precipitation in Europe derived from a combination of dynamical and statistical approaches. *Int. J. Climatol.* **2020**, *40*, 4800–4827. [CrossRef]
231. Hou, A.Y.; Kakar, R.K.; Neeck, S.; Azarbarzin, A.A.; Kummerow, C.D.; Kojima, M.; Oki, R.; Nakamura, K.; Iguchi, T. The Global Precipitation Measurement Mission. *Bull. Am. Meteorol. Soc.* **2014**, *95*, 701–722. [CrossRef]
232. Levizzani, V.; Cattani, E. Satellite Remote Sensing of Precipitation and the Terrestrial Water Cycle in a Changing Climate. *Remote Sens.* **2019**, *11*, 2301. [CrossRef]

233. Covello, F.; Battazza, F.; Coletta, A.; Lopinto, E.; Fiorentino, C.; Pietranera, L.; Valentini, G.; Zoffoli, S. COSMO_SkyMed an existing opportunity for observing the Earth. *J. Geodyn.* **2010**, *49*, 171–180. [CrossRef]
234. Caltagirone, F.; Capuzzi, A.; Coletta, A.; De Luca, G.F.; Scorzafava, E.; Leonardi, R.; Rivola, S.; Fagioli, S.; Angino, G.; L'Abbate, M.; et al. The COSMO-SkyMed Dual Use Earth Observation Program: Development, Qualification, and Results of the Commissioning of the Overall Constellation. *IEEE J. Sel. Top. Appl. Earth Obs. Remote Sens.* **2014**, *7*, 2754–2762. [CrossRef]
235. Battaglia, A.; Kollias, P.; Dhillon, R.; Roy, R.; Tanelli, S.; Lamer, K.; Grecu, M.; Lebsock, M.; Watters, D.; Mroz, K.; et al. Spaceborne cloud and precipitation radars: Status, challenges, and ways forward. *Rev. Geophys.* **2020**, *58*, e2019RG000686. [CrossRef]
236. Li, N.; Wang, Z.; Chen, X.; Austin, G. Studies of General Precipitation Features with TRMM PR Data: An Extensive Overview. *Remote Sens.* **2019**, *11*, 80. [CrossRef]
237. Panegrossi, G.; Casella, D.; Dietrich, S.; Marra, A.C.; Sanò, P.; Mugnai, A.; Baldini, L.; Roberto, N.; Adirosi, E.; Cremonini, R.; et al. Use of the GPM constellation for monitoring heavy precipitation events over the Mediterranean region. *IEEE J. Sel. Top. Appl. Earth Obs. Remote Sens.* **2016**, *9*, 2733–2753. [CrossRef]
238. Yong, B.; Liu, D.; Gourley, J.J.; Tian, Y.; Huffman, G.J.; Ren, L.; Hong, Y. Global View Of Real-Time TRMM Multisatellite Precipitation Analysis: Implications For Its Successor Global Precipitation Measurement Mission. *Bull. Am. Meteorol. Soc.* **2015**, *96*, 283–296. [CrossRef]
239. McCabe, M.F.; Rodell, M.; Alsdorf, D.E.; Miralles, D.G.; Uijlenhoet, R.; Wagner, W.; Lucieer, A.; Houborg, R.; Verhoest, N.E.C.; Franz, T.E.; et al. The future of Earth Observation in hydrology. *Hydrol. Earth Syst. Sci.* **2017**, *21*, 3879–3914. [CrossRef]
240. Caspi, A.; Barthelemy, M.; Bussy-Virat, C.D.; Cohen, I.J.; DeForest, C.E.; Jackson, D.R.; Vourlidas, A.; Nieves-Chinchilla, T. Small satellite mission concepts for space weather research and as pathfinders for operations. *Space Weather* **2022**, *20*, e2020SW002554. [CrossRef]
241. Berg, W.; Brown, S.T.; Lim, B.H.; Reising, S.C.; Goncharenko, Y.; Kummerow, C.D.; Gaier, T.C.; Padmanabhan, S. Calibration and Validation of the TEMPEST-D CubeSat Radiometer. *IEEE Trans. Geosci. Remote Sens.* **2021**, *59*, 4904–4914. [CrossRef]
242. Blackwell, W.J.; Braun, S.; Bennartz, R.; Velden, C.; DeMaria, M.; Atlas, R.; Dunion, J.; Marks, F.; Rogers, R.; Annane, B.; et al. An overview of the TROPICS NASA Earth Venture Mission. *Q. J. R Meteorol. Soc.* **2018**, *144* (Suppl. S1), 16–26. [CrossRef]
243. Mehta, A.V.; Yang, S. Precipitation climatology over Mediterranean Basin from ten years of TRMM Measurement. *Adv. Geosci.* **2008**, *17*, 87–91. [CrossRef]
244. Murphy, M.S.; Konrad, C.E., II. Spatial and Temporal Patterns of Thunderstorm Events that Produce Cloud-to-Ground Lightning in the Interior Southeastern United States. *Mon. Weather Rev.* **2005**, *133*, 1417–1430. [CrossRef]
245. Retalis, A.; Katsanos, D.; Michaelides, S. Precipitation climatology over the Mediterranean Basin—Validation over Cyprus. *Atmos. Res.* **2016**, *169*, 449–458. [CrossRef]
246. Stampoulis, D.; Emmanouil, N.A. Assessment of High-Resolution Satellite-Based Rainfall Estimates over the Mediterranean during Heavy Precipitation Events. *J. Hydrometeorol.* **2013**, *14*, 1500–1514. [CrossRef]
247. Ruf, C.S.; Chew, C.; Lang, T.; Morris, M.G.; Nave, K.; Ridley, A.; Balasubramaniam, R. A New Paradigm in Earth Environmental Monitoring with the CYGNSS Small Satellite Constellation. *Sci. Rep.* **2018**, *8*, 8782. [CrossRef] [PubMed]
248. Baldini, L.; Chandrasekar, V.; Moisseev, D. Microwave radar signatures of precipitation from S band to Ka band: Application to GPM mission. *Eur. J. Remote Sens.* **2012**, *45*, 75–88. [CrossRef]
249. Kirstetter, P.-E.; Andrieu, H.; Delrieu, G.; Boudevillain, B. Identification of Vertical Profiles of Reflectivity for Correction of Volumetric Radar Data Using Rainfall Classification. *J. Appl. Meteorol. Clim.* **2010**, *49*, 2167–2180. [CrossRef]
250. Friedrich, K.; Hagen, M.; Einfalt, T. A Quality Control Concept for Radar Reflectivity, Polarimetric Parameters, and Doppler Velocity. *J. Atmos. Ocean. Tech.* **2006**, *23*, 865–887. [CrossRef]
251. Martins Costa do Amaral, L.; Barbieri, S.; Vila, D.; Puca, S.; Vulpiani, G.; Panegrossi, G.; Biscaro, T.; Sanò, P.; Petracca, M.; Marra, A.C.; et al. Assessment of Ground-Reference Data and Validation of the H-SAF Precipitation Products in Brazil. *Remote Sens.* **2018**, *10*, 1743. [CrossRef]
252. Qi, Y.; Zhang, J.; Zhang, P. A real-time automated convective and stratiform precipitation segregation algorithm in native radar coordinates. *Q. J. R. Meteor. Soc.* **2013**, *193*, 2233–2240. [CrossRef]
253. Chaturvedi, S.K. Study of synthetic aperture radar and automatic identification system for ship target detection. *J. Ocean Eng. Sci.* **2019**, *4*, 173–182. [CrossRef]
254. Moreira, A.; Prats-Iraola, P.; Younis, M.; Krieger, G.; Hajnsek, I.; Papathanassiou, K.P. A tutorial on synthetic aperture radar. *IEEE Geosci. Remote Sens. Mag.* **2013**, *1*, 6–43. [CrossRef]
255. Crisp, D.J. The State-of-the-Art in Ship Detection in Synthetic Aperture Radar Imagery. Defence Sci. Technol. Org., Port Wakefield, South Australia, 2004, Research Report DSTO-RR-0272. Available online: http://www.dsto.defence.gov.au/corporate/reports (accessed on 26 September 2021).
256. Ouchi, K. Current Status on Vessel Detection and Classification by Synthetic Aperture Radar for Maritime Security and Safety. In Proceedings of the 38th Symposium on Remote Sensing for Environmental Sciences, Gamagori, Aichi, Japan, 3–5 September 2016; pp. 5–12.
257. Pelich, R.; Longépé, N.; Mercier, G.; Hajduch, G.; Garello, R. Performance evaluation of Sentinel-1 data in SAR ship detection. In Proceedings of the 2015 IEEE International Geoscience and Remote Sensing Symposium (IGARSS), Milan, Italy, 26–31 July 2015. [CrossRef]

258. Snapir, B.; Waine, T.W.; Biernamnn, L. Maritime Vessel Classification to Monitor Fisheries with SAR: Demonstration in the North Sea. *Remote Sens.* **2019**, *11*, 353. [CrossRef]
259. Buckreuss, S.; Schättler, B.; Fritz, T.; Mittermayer, J.; Kahle, R.; Maurer, E.; Böer, J.; Bachmann, M.; Mrowka, F.; Schwarz, E.; et al. Ten Years of TerraSAR-X Operations. *Remote Sens.* **2018**, *10*, 873. [CrossRef]
260. Brusch, S.; Lehner, S.; Fritz, T.; Soccorsi, M.; Soloviev, A.; van Schie, B. Ship Surveillance With TerraSAR-X. *IEEE Trans. Geosci. Remote Sens.* **2011**, *49*, 1092–1103. [CrossRef]
261. Marin, C.; Bovolo, F.; Bruzzone, L. Building Change Detection in Multitemporal Very High Resolution SAR Images. *IEEE Trans. Geosci. Remote Sens.* **2015**, *53*, 2664–2682. [CrossRef]
262. Bovolo, F.; Marin, C.; Bruzzone, L. A Hierarchical Approach to Change Detection in Very High Resolution SAR Images for Surveillance Applications. *IEEE Trans. Geosci. Remote Sens.* **2013**, *51*, 2042–2054. [CrossRef]
263. Lanz, P.; Marino, A.; Brinkhoff, T.; Köster, F.; Möller, M. The InflateSAR Campaign: Testing SAR Vessel Detection Systems for Refugee Rubber Inflatables. *Remote Sens.* **2021**, *13*, 1487. [CrossRef]
264. Migliaccio, M.; Gambardella, A.; Nunziata, F. Ship detection over single-look complex SAR images. In Proceedings of the IEEE/OES US/EU-Baltic International Symposium, Tallinn, Estonia, 27–29 May 2008. [CrossRef]
265. Schwartz, C.; Ramos, L.P.; Duarte, L.T.; da S. Pinho, M.; Pettersson, M.I.; Vu, V.T.; Machado, R. Change Detection in UWB SAR Images Based on Robust Principal Component Analysis. *Remote Sens.* **2020**, *12*, 1916. [CrossRef]
266. Gambardella, A.; Nunziata, F.; Migliaccio, M. A Physical Full-Resolution SAR Ship Detection Filter. *IEEE Geosci. Remote Sens. Lett.* **2008**, *5*, 760–763. [CrossRef]
267. Migliaccio, M.; Ferrara, G.; Gambardella, A.; Nunziata, F.; Sorrentino, A. A Physically Consistent Speckle Model for Marine SLC SAR Images. *IEEE J. Ocean. Eng.* **2007**, *32*, 839–847. [CrossRef]
268. Wang, Y.; Liu, H. A hierarchical Ship Detection Scheme for High-Resolution SAR images. *IEEE Trans. Geosci. Remote Sens.* **2012**, *50*, 4173–4184. [CrossRef]
269. Saha, S.; Bovolo, F.; Bruzzone, L. Destroyed-buildings detection from VHR SAR images using deep features. In Proceedings of the Image and Signal Processing for Remote Sensing XXIV, Berlin, Germany, 10–13 September 2018; Volume 10789, p. 107890Z. [CrossRef]
270. Pennino, S.; Angrisano, A.; Della Corte, V.; Ferraioli, G.; Gaglione, S.; Innac, A.; Martellato, E.; Palumbo, P.; Piscopo, V.; Rotundi, A.; et al. Sea State Monitoring by Ship Motion Measurements Onboard a Research Ship in the Antarctic Waters. *J. Mar. Sci. Eng.* **2021**, *9*, 64. [CrossRef]
271. Pascoal, R.; Guedes Soares, C.; Sørensen, J. Ocean wave spectral estimation using vessel wave frequency motions. *J. Offshore Mech. Arct. Eng.* **2007**, *129*, 90–96. [CrossRef]
272. Piscopo, V.; Scamardella, A.; Gaglione, S. A new wave spectrum resembling procedure based on ship motion analysis. *Ocean Eng.* **2020**, *201*, 107137. [CrossRef]
273. Krata, P.; Szlapczynska, J. Weather hazard avoidance in modeling safety of motor-driven ship for multicriteria weather routing. *Int. J. Mar. Navig. Saf. Sea Transp.* **2012**, *6*, 71–78. [CrossRef]
274. Scamardella, A.; Piscopo, V. Passenger ship seakeeping optimization by the Overall Motion Sickness Incidence. *Ocean Eng.* **2014**, *76*, 86–97. [CrossRef]
275. Born, G.H.; Dunne, J.A.; Lame, D.B. Seat Mission Overview. *Science* **1979**, *204*, 1405–1406. [CrossRef] [PubMed]
276. Geudtner, D.; Tossaint, M.; Davidson, M.; Torres, R. Copernicus Sentinel-1 Next Generation Mission. In Proceedings of the IEEE International Geoscience ad Remote Sensing Symposium IGARSS, Brussels, Belgium, 11–16 July 2021; pp. 874–876. [CrossRef]
277. Bruck, M.; Lehner, S. Coastal wave field extraction using TerraSAR-X data. *J. Appl. Remote Sens.* **2013**, *7*, 073694. [CrossRef]
278. Pleskachevsky, A.; Jacobse, S.; Tings, B.; Schwarz, E. Estimation of sea state from Sentinel-1 Synthetic aperture radar imagery for maritime situation awareness. *Int. J. Remote Sens.* **2019**, *40*, 4104–4142. [CrossRef]
279. Innac, A.; Angrisano, A.; Dardanelli, G.; Della Corte, V.; Martellato, E.; Rotundi, A.; Ferraioli, G.; Palumbo, P.; Gaglione, S. A Kalman filter single point positioning for maritime applications using a smartphone. *Geogr. Tech.* **2021**, *16*, 15–29. [CrossRef]
280. Montazeri, N.; Nielsen, U.D.; Jensen, J.J. Estimation of wind sea and swell using shipboard measurements—A refined parametric modelling approach. *Appl. Ocean Res.* **2016**, *54*, 73–86. [CrossRef]
281. Chupin, C.; Ballu, V.; Testut, L.; Tranchant, Y.-T.; Calzas, M.; Poirier, E.; Coulombier, T.; Laurain, O.; Bonnefond, P.; Team FOAM Project. Mapping Sea Surface Height Using New Concepts of Kinematic GNSS Instruments. *Remote Sens.* **2020**, *12*, 2656. [CrossRef]
282. Foster, J.H.; Carter, G.S.; Merrifield, M.A. Ship-based measurements of sea surface topography. *Geophys. Res. Lett.* **2009**, *36*, L11605. [CrossRef]
283. Pascoal, R.; Perera, L.P.; Soares, C.G. Estimation of directional spectra from ship motions sea trials. *Ocean Eng.* **2017**, *132*, 126–137. [CrossRef]
284. Dalla Mura, M.; Prasad, S.; Pacifici, F.; Gamba, P.; Chanussot, J.; Benediktsson, J.A. Challenges and Opportunities of Multimodality and Data Fusion in Remote Sensing. *Proc. IEEE* **2015**, *103*, 1585–1601. [CrossRef]
285. Ghassemian, H. A review of remote sensing image fusion methods. *Inform. Fusion.* **2016**, *32*, 75–89. [CrossRef]
286. Ghamisi, P.; Rasti, B.; Yokoya, N.; Wang, Q.; Höfle, B.; Bruzzone, L.; Bovolo, F.; Chi, M.; Anders, K.; Gloaguen, R.; et al. Multisource and Multitemporal Data Fusion in Remote Sensing: A Comprehensive Review of the State of the Art. *IEEE Geosci. Remote Sens. Mag.* **2019**, *7*, 6–39. [CrossRef]

287. Belgiu, M.; Stein, A. Spatiotemporal Image Fusion in Remote Sensing. *Remote Sens.* **2019**, *11*, 818. [CrossRef]
288. Zhang, J. Multi-source remote sensing data fusion: Status and trends. *Int. J. Image Data Fusion.* **2010**, *1*, 5–24. [CrossRef]
289. Castanedo, F. A review of data fusion techniques. *Sci. World J.* **2013**, *2013*, 704504. [CrossRef]
290. Arun, P.V.; Sadeh, R.; Avneri, A.; Tubul, Y.; Camino, C.; Buddhiraju, K.M.; Porwal, A.; Lati, R.N.; Zarco-Tejada, P.J.; Peleg, Z.; et al. Multimodal Earth Observation data fusion: Graph-based approach in shared latent space. *Inform. Fusion* **2022**, *78*, 20–39. [CrossRef]
291. Rodger, M.; Guida, R. Classification-Aided SAR and AIS Data Fusion for Space-Based Maritime Surveillance. *Remote Sens.* **2021**, *13*, 104. [CrossRef]
292. Zhang, J.; Zhou, Y.; Luo, J. Deep learning for processing and analysis of remote sensing big data: A technical review. *Big Earth Data* **2021**. [CrossRef]
293. Keenan, T.F.; Davidson, E.; Moffat, A.M.; Munger, W.; Richardson, A.D. Using model-data fusion to interpret past trends, and quantify uncertainties in future projections, of terrestrial ecosystem carbon cycling. *Glob. Chang. Biol.* **2012**, *18*, 2555–2569. [CrossRef]
294. Fernández Prieto, D. Change detection in multisensor remote-sensing data for desertification monitoring. In Proceedings of the Third International Symposium on Retrieval of Bio- and Geophysical Parameters from SAR Data for Land Applications, Sheffield, UK, 11–14 September 2001; Wilson, A., Quegan, S., Eds.; ESA SP-475; ESA Publications Division: Noordwijk, The Netherlands, 2002; pp. 255–260.
295. Schultz, M.; Clevers, J.G.P.W.; Carter, S.; Verbesselt, J.; Avitabile, V.; Quang, H.V.; Herold, M. Performance of vegetation indices from Landsat time series in deforestation monitoring. *Int. J. Appl. Earth Obs.* **2016**, *52*, 318–327. [CrossRef]
296. Basile, M.; Maglione, P.; Parente, C.; Santamaria, R. Cartography and remote sensing for coastal erosion analysis. Coastal Processes II. *WIT Trans. Ecol. Environ.* **2011**, *149*, 65–76. [CrossRef]
297. Hu, Y.; Jia, G.; Pohl, C.; Feng, Q.; He, Y.; Gao, H.; Xu, R.; van Genderen, J.; Feng, J. Improved monitoring of urbanization processes in China for regional climate impact assessment. *Environ. Earth Sci.* **2015**, *73*, 8387–8404. [CrossRef]
298. Ehlers, M.; Klonus, S.; Åstrand, P.J.; Rosso, P. Multi-sensor image fusion for pansharpening in remote sensing. *Int. J. Image Data Fusion* **2010**, *1*, 25–45. [CrossRef]
299. Garzelli, A. A Review of Image Fusion Algorithms Based on the Super-Resolution Paradigm. *Remote Sens.* **2016**, *8*, 797. [CrossRef]
300. Palubinskas, G. Fast, simple, and good pan-sharpening method. *J. Appl. Remote Sens.* **2013**, *7*, 073526. [CrossRef]
301. Bork, E.W.; Su, J.G. Integrating LIDAR data and multispectral imagery for enhanced classification of rangeland vegetation: A meta analysis. *Remote Sens. Environ.* **2007**, *111*, 11–24. [CrossRef]
302. Bovolo, F.; Bruzzone, L. The Time Variable in Data Fusion: A Change Detection Perspective. *IEEE Geosci. Remote Sens. Mag.* **2015**, *3*, 8–26. [CrossRef]
303. Alcaras, E.; Parente, C.; Vallario, A. Automation of Pan-Sharpening Methods for Pléiades Images Using GIS Basic Functions. *Remote Sens.* **2021**, *13*, 1550. [CrossRef]
304. Alcaras, E.; Della Corte, V.; Ferraioli, G.; Martellato, E.; Palumbo, P.; Parente, C.; Rotundi, A. Comparison of Different Pan-sharpening Methods applied to IKONOS Imagery. *Geog. Tech.* **2021**, *16*, 198–210. [CrossRef]
305. Da Deppo, V.; Martellato, E.; Simioni, E.; Naletto, G.; Cremonese, G. Radiometric model for the stereo camera STC onboard the BepiColombo ESA mission. In Proceedings of the Modeling, Systems Engineering, and Project Management for Astronomy VII, Edinburgh, UK, 26 June–1 July 2016; Volume 9911, p. 99111T. [CrossRef]
306. Cremonese, G.; Capaccioni, F.; Capria, M.T.; Doressoundiram, A.; Palumbo, P.; Vincendon, M.; Massironi, M.; Debei, S.; Zusi, M.; Altieri, F.; et al. SIMBIO-SYS: Scientific Cameras and Spectrometer for the BepiColombo Mission. *Space Sci. Rev.* **2020**, *216*, 75. [CrossRef]
307. NASA/GSFC—Courtesy of Parkinson, C.L., Aqua Brochure, 2002, #NP-2002-1-422-GSFC. Available online: https://www.nasa.gov/pdf/151986main_Aqua_brochure.pdf (accessed on 18 September 2021).
308. Stephens, G.L.; Vane, D.G.; Boain, R.J.; Mace, G.G.; Sassen, K.; Wang, Z.; Illingworth, A.J.; O'connor, E.J.; Rossow, W.B.; Durden, S.L.; et al. The Cloudsat mission and the A-Train: A new dimension of space-based observations of clouds and precipitation. *Am. Meteorol. Soc.* **2002**, *83*, 1771–1790. [CrossRef]
309. NTRS-NASA Technical Reports Server, Science Requirements Document for OMI-EOS. 2000; 194p. Available online: https://ntrs.nasa.gov/citations/20010082524 (accessed on 18 September 2021).
310. Italian Space Agency. COSMO-SkyMed Mission and Products Description, 2019, #ASI-CSM-PMG-NT-001, Rev. 3, 151p. Available online: https://www.asi.it/wp-content/uploads/2019/08/COSMO-SkyMed-Mission-and-Products-Description_rev3-2.pdf (accessed on 18 September 2021).
311. Italian Space Agency. COSMO-SkyMed Seconda Generazione: System and Products Description, 2021, #CE-UOT-2021-002, 217p. Available online: https://www.asi.it/wp-content/uploads/2021/03/CSG-Mission-and-Products-Description-defpdf.pdf (accessed on 18 September 2021).
312. JPSS Pr307ogram Office Website. Available online: https://www.nesdis.noaa.gov/about/our-offices/joint-polar-satellite-system-jpss-program-office (accessed on 18 September 2021).
313. IASI Website. Available online: https://iasi.cnes.fr/en/IASI/index.htm (accessed on 18 September 2021).
314. Sentinel Website. Available online: https://sentinel.esa.int/web/sentinel/home (accessed on 18 September 2021).

315. Royal Netherlands Meteorological Institute. Algorith Theoretical Basis Document for the TROPOMI L01b Data Processor. 2019. #S5P-KNMI-L01B-0009-SD, 186p. Available online: https://sentinel.esa.int/documents/247904/2476257/Sentinel-5P-TROPOMI-Level-1B-ATBD (accessed on 18 September 2021).
316. MAXAR. WorldView-1, MXR-DS-wv1 06/20. Available online: https://resources.maxar.com/data-sheets/worldview-1 (accessed on 18 September 2021).
317. MAXAR. WorldView-3, MXR-DS-wv3 08/20. Available online: https://resources.maxar.com/data-sheets/worldview-3 (accessed on 18 September 2021).